

The Star-forming Main Sequence of the Host Galaxies of Low-redshift Quasars

MING-YANG ZHUANG (庄明阳) ^{1,2} AND LUIS C. HO ^{1,2}

¹Kavli Institute for Astronomy and Astrophysics, Peking University, Beijing 100871, China

²Department of Astronomy, School of Physics, Peking University, Beijing 100871, China

Submitted to ApJ

ABSTRACT

We investigate the star-forming main sequence of the host galaxies of a large, well-defined sample of 453 redshift ~ 0.3 quasars with previously available star formation rates by deriving stellar masses from modeling their broad-band (*grizy*) spectral energy distribution. We perform two-dimensional, simultaneous, multi-filter decomposition of Pan-STARRS1 3π Steradian Survey images to disentangle the active galactic nucleus (AGN) from its host galaxy, by explicitly considering, for the first time, the wavelength variation of galaxy structures. We quantify the Sérsic profiles and sizes of the host galaxies from mock AGNs generated from both real and idealized galaxies. Detailed morphological classifications of the calibration galaxy sample with Hubble Space Telescope images enable us to estimate crude morphological types of the quasars. Although the majority ($\sim 60\%$) of the quasars are hosted by bulge-dominated, early-type galaxies, a substantial fraction ($\sim 40\%$) reside in disk-dominated, late-type galaxies, suggesting that at least in these systems major mergers have not played a significant role in regulating their AGN activity, in agreement with recent simulations and observations of nearby quasars. The vast majority ($\sim 90\%$) of the quasars have star formation rates that place them on or above the galaxy star-forming main sequence, with more rapidly accreting AGNs displaced further above the main sequence. Quasar host galaxies generally follow the stellar mass-size relation defined by inactive galaxies, both for late-type and early-type systems, but roughly 1/3 of the population has smaller sizes at a given stellar mass, reminiscent of compact star-forming galaxies at higher redshift.

Keywords: Active galactic nuclei(16) — Galaxy evolution(594) — Galaxy structure(622) — Quasars (1319) — Supermassive black holes(1663) — AGN host galaxies(2017)

1. INTRODUCTION

The discovery of tight correlations between the masses of supermassive black holes (BHs) and the properties of their host galaxies suggests that BHs coevolve with galaxies (e.g., Magorrian et al. 1998; Richstone et al. 1998; Gebhardt et al. 2000; Ferrarese & Merritt 2000; Ho 2004; Kormendy & Ho 2013; Heckman & Best 2014). What dictates their joint evolution? How were the correlations between BH mass (M_{BH}) and host galaxy properties established? Popular scenarios suggest that active galactic nuclei (AGNs) play a significant role in this narrative by injecting energy and momentum into their environment. The feedback produced by AGNs in the form of fast outflows or jets acts as a double-edged sword for their host galaxies. On the one hand, they are

expected to prevent cooling of intergalactic gas by relativistic jets that inflate large-scale cavities (radio/kinetic mode; e.g., Brüggén & Kaiser 2002; McNamara & Nulsen 2007) and expel gas in the interstellar medium by radiatively driven outflows (quasar/radiative mode; e.g., Di Matteo et al. 2005; Hopkins et al. 2008; Feruglio et al. 2010) and hence suppress star formation (negative feedback). On the other hand, outflows can compress ambient gas and directly induce in situ star formation in the outflows themselves (positive feedback; e.g., Zubovas et al. 2013; Maiolino et al. 2017; Gallagher et al. 2019; Qiu et al. 2020). Positive and negative feedback are not necessarily mutually exclusive; they have been found to occur within the same galaxy at the same time (e.g., Cresci et al. 2015; Shin et al. 2019; Mandal et al. 2021).

Star-forming galaxies, both in the local and distant Universe, follow a main sequence (MS), a tight correlation between star formation rate (SFR) and stellar mass (e.g.,

Brinchmann et al. 2004; Elbaz et al. 2011; Speagle et al. 2014; Renzini & Peng 2015). In principle, the galaxy star-forming MS offers an effective framework to advance our understanding of the impact of AGNs on galaxy evolution. By comparing galaxies at fixed stellar mass, especially if other conditions such as gas fraction and morphology can be specified, the position of AGN hosts relative to the MS informs us of the degree and manner in which BH accretion-related processes influence star formation. However, the current observational landscape is quite complex. Nearby, low-luminosity AGNs mainly lie in the green valley (e.g., Salim et al. 2007; Leslie et al. 2016), the sparsely populated region with reduced SFR below the MS, or are altogether quiescent (Ho et al. 2003). By contrast, their more luminous counterparts, the quasars, can be found below (e.g., Shimizu et al. 2015; Stemo et al. 2020), on (e.g., Husemann et al. 2014; Woo et al. 2017; Smirnova-Pinchukova et al. 2022), or even above (e.g., Jarvis et al. 2020; Shangguan et al. 2020b; Xie et al. 2021; Koutoulidis et al. 2022) the star-forming galaxy MS. Several factors contribute to this confusing status of affairs, including the wavelength used for sample selection (X-ray, optical, infrared, or radio), the methodology and uncertainties associated with SFR and stellar mass determination, and even the very shape and normalization of the MS used for reference comparison. Recent works suggest that the position of an AGN relative to the MS is correlated with Eddington ratio (e.g., Shimizu et al. 2015; Ellison et al. 2016; Woo et al. 2020; Torbaniuk et al. 2021), with higher SFRs found in hosts of AGNs with higher Eddington ratio.

A practical difficulty is that the emission from rapidly accreting BHs (Eddington ratio $\lambda_E \gtrsim 10^{-3}$)¹ in type 1 AGNs can easily dominate the observed spectral energy distribution (SED) of the host galaxy starlight at ultraviolet, optical, and near-infrared wavelengths, posing a major obstacle to obtaining reliable information on the stellar mass and SFR of the galaxy. To address these challenges, much attention has been devoted to deriving accurate SFRs for AGN host galaxies. Efforts include the development of comprehensive AGN dust emission models (e.g., Hönig & Kishimoto 2017; Stalevski et al. 2019), new or improved emission-line diagnostics based on empirical methods and photoionization modeling (e.g., Ho 2005; Kim et al. 2006; Thomas et al. 2018; Zhuang & Ho 2019; Zhuang et al. 2019), mid-infrared polycyclic aromatic hydrocarbon features and the far-infrared continuum (Xie et al. 2021), and modern SED fitting codes incorporating sophisticated models (e.g., Calistro Rivera et al. 2016; Zhuang et al. 2018; Yang et al. 2020).

This paper focuses on the equally pressing issue of how to derive stellar masses for type 1 AGNs. In inactive galaxies, stellar mass can be inferred by comparing galaxy spectra or multi-band integrated photometry with stellar population and dust attenuation models (e.g., Bell et al. 2003; Conroy 2013). Active galaxies require the additional complicated step of deblending the AGN from the host. Several strategies have been pursued, including direct broadband SED fitting using AGN and stellar templates (e.g., Merloni et al. 2010; Ciesla et al. 2015; Suh et al. 2019), detailed spectral modeling of the spectrum using stellar absorption features (e.g., Vanden Berk et al. 2006; Matsuoka et al. 2015), and photometric analysis after AGN-host image decomposition (e.g., Matsuoka et al. 2014; Bentz & Manne-Nicholas 2018; Yue et al. 2018; Ishino et al. 2020; Bennert et al. 2021; Li et al. 2021a; Zhao et al. 2021). A practical difficulty, however, is that in the most powerful quasars the integrated spectrum will be completely overwhelmed by the nucleus, barely leaving room for the starlight to be detected in the residuals. In this regard, image decomposition offers a distinct advantage by exploiting the inherently different spatial distribution of the physical components: whereas the host galaxy spans a wide range of physical scales and can comprise multiple subcomponents, the active nucleus is uniquely localized in (or near) the galaxy center, and its light distribution follows the point-spread function (PSF) of the image. These priors can be used to one’s advantage to decouple the AGN from its host.

Measuring the stellar mass, nevertheless, is more challenging than simply detecting the light. To estimate the stellar mass requires photometry in at least two bands with sufficient wavelength separation to yield, at the bare minimum, a rudimentary color, which can be used to constrain the age and hence mass-to-light ratio of the stellar population. Previous studies of bright AGNs derive mainly from relatively small samples of high-resolution imaging with the Hubble Space Telescope (HST), usually acquired in only one filter, or at most a very small number of filters (McLure et al. 1999; Dunlop et al. 2003; Greene et al. 2008; Kim et al. 2008; Jiang et al. 2011; Zhao et al. 2021). Consequently, most investigations have focused on the relation between BH mass and host galaxy stellar luminosity, not stellar mass. To compare with the local scaling relation, one needs to assume a certain galaxy evolution model to obtain the equivalent galaxy luminosity at redshift 0 (e.g., Peng et al. 2006), which unavoidably introduces more uncertainties. In the largest HST sample assembled to date, Kim et al. (2017) studied 235 low-redshift (< 0.35) type 1 AGNs of heterogeneous origin from the data archives, for which they have only single-band photometry. This necessarily limits the physical interpretation of the sample (Kim & Ho 2019). Large ground-based imaging surveys can furnish multi-band information more readily, but at the expense of lower spatial resolution. Previ-

¹ We define the Eddington ratio as $\lambda_E \equiv L_{\text{bol}}/L_E$, with L_{bol} the bolometric luminosity and $L_E = 1.26 \times 10^{38} (M_{\text{BH}}/M_{\odot})$ the Eddington luminosity.

ous works using images from Stripe 82 (Annis et al. 2014) of the Sloan Digital Sky Survey (SDSS; York et al. 2000) have shown that it is possible to decompose AGN host galaxies up to redshift ~ 0.6 (e.g., Falomo et al. 2014; Matsuoka et al. 2014). With the advent of deeper, higher resolution data from the Hyper Suprime-Cam Subaru Strategic Program (Aihara et al. 2018), AGN image decomposition from ground-based surveys has been pushed to redshift ~ 1 (Ishino et al. 2020; Li et al. 2021a).

Host galaxy parameters can be extracted from either one-dimensional parametric fits of the azimuthally averaged radial surface brightness profile or decomposition of the two-dimensional image itself. The popular two-dimensional image decomposition code GALFIT (Peng et al. 2002, 2010) can model simultaneously a variety of galaxy substructures besides the traditional bulge and disk, including bars, lenses, rings, and spiral arms, as well as close companions. More recent softwares (e.g., Imfit: Erwin 2015; ProFit: Robotham et al. 2017; lenstronomy: Birrer & Amara 2018) offer a Bayesian framework to enable more reliable error estimates. When more than one band is available, it is common practice, for the purposes of minimizing parameter degeneracy, to fix the structure of the galaxy to that determined from the band with best resolution, highest signal-to-noise ratio, and most optimal host-to-AGN contrast ratio (e.g., Matsuoka et al. 2014; Yue et al. 2018; Ding et al. 2020; Li et al. 2021a,b; Zhao et al. 2021). However, the morphology and structure of a galaxy can vary significantly with wavelength owing to variations in stellar population, metallicity gradient, or dust attenuation. For example, a spiral galaxy tends to have brighter disk emission at shorter wavelengths and a more prominent bulge component at longer wavelengths, such that the galaxy looks more extended and flatter toward the ultraviolet and more compact and steeper in the near-infrared. In their decomposition of multiwavelength images of nearby galaxies, Kelvin et al. (2012) find that the Sérsic (1968) index increases while the half-light radius decreases toward longer wavelengths. To our knowledge, no work has taken the wavelength dependence of galaxy structure into consideration when performing AGN host galaxy decomposition, even though this capability is possible (e.g., GALFITM; Häußler et al. 2013; Vika et al. 2013). Neglecting this phenomenon introduces unknown systematic biases.

Zhuang & Ho (2020) constructed a well-defined sample of 453 redshift $0.3 - 0.35$ unobscured AGNs (hereinafter, the redshift ~ 0.3 quasar sample), based on the presence of broad $H\alpha$ emission in SDSS spectra, primarily for the purposes of investigating their star formation properties. The 3π Steradian Survey of Pan-STARRS1 (PS1; Chambers et al. 2016)

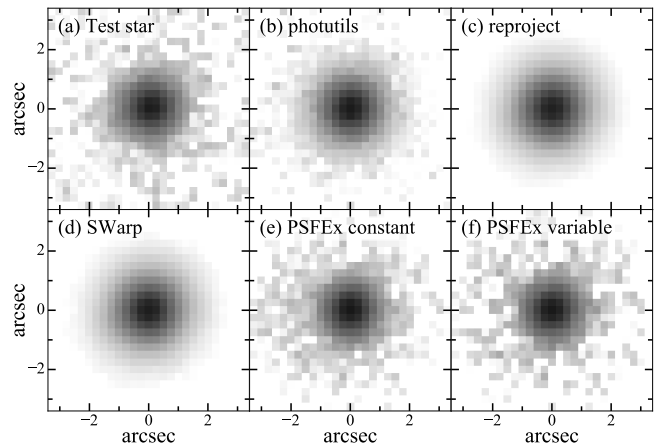


Figure 1. An example of a test star ($m = 18.8$ mag; panel a) and five PSF models (panels b–f) generated using all other stars in the i -band image of SDSS J021652.47–002335.3 ($m_{\text{PSF}} = 18.2$ mag). Test stars are selected to be within 1 mag of the PSF magnitude of the AGN. PSF models are generated using photutils, reproject, SWarp, and PSFEx are shown in panels b–f. PSFEx provides two versions of PSF models: position-constant (PSFEx constant) and position-variable (PSFEx variable); for the latter, we consider a second-order polynomial variation on pixel coordinates.

conveniently provides five-band² (*grizy*) images for the entire sample, with better red sensitivity and improved spatial resolution compared to SDSS. The large sample size and rich ancillary information, which includes SFR, BH mass, and molecular gas mass estimated using dust attenuation (Zhuang et al. 2021) make this sample ideal to study the coevolution between supermassive BHs and their host galaxies. In this paper, we perform two-dimensional decomposition of the PS1 images of the redshift ~ 0.3 quasar sample, with the primary goal of deriving their structural properties and stellar masses. Section 2 introduces the sample and data, and performs an extensive investigation of the PSF models needed for the analysis. In Section 3, we present the two-dimensional multiwavelength simultaneous decomposition and verify our results using mock data. We fit the AGN-decomposed galaxy SED to derive stellar masses and use structural parameters to obtain morphological classifications (Section 4). Section 5 discusses the physical properties of AGN host galaxies in the context of the galaxy star-forming MS, and the triggering mechanism of AGNs. Our main conclusions are summarized in Section 6. This work adopts a cosmology with $H_0 = 70 \text{ km s}^{-1} \text{ Mpc}^{-1}$, $\Omega_m = 0.3$, and $\Omega_\Lambda = 0.7$. Stellar masses and SFRs assume the initial mass function of Kroupa (2001).

² The five filters employed by PS1 officially are designated g_{P1} , r_{P1} , i_{P1} , z_{P1} , and y_{P1} . For brevity, hereinafter we simply refer to them without the “P1” subscript.

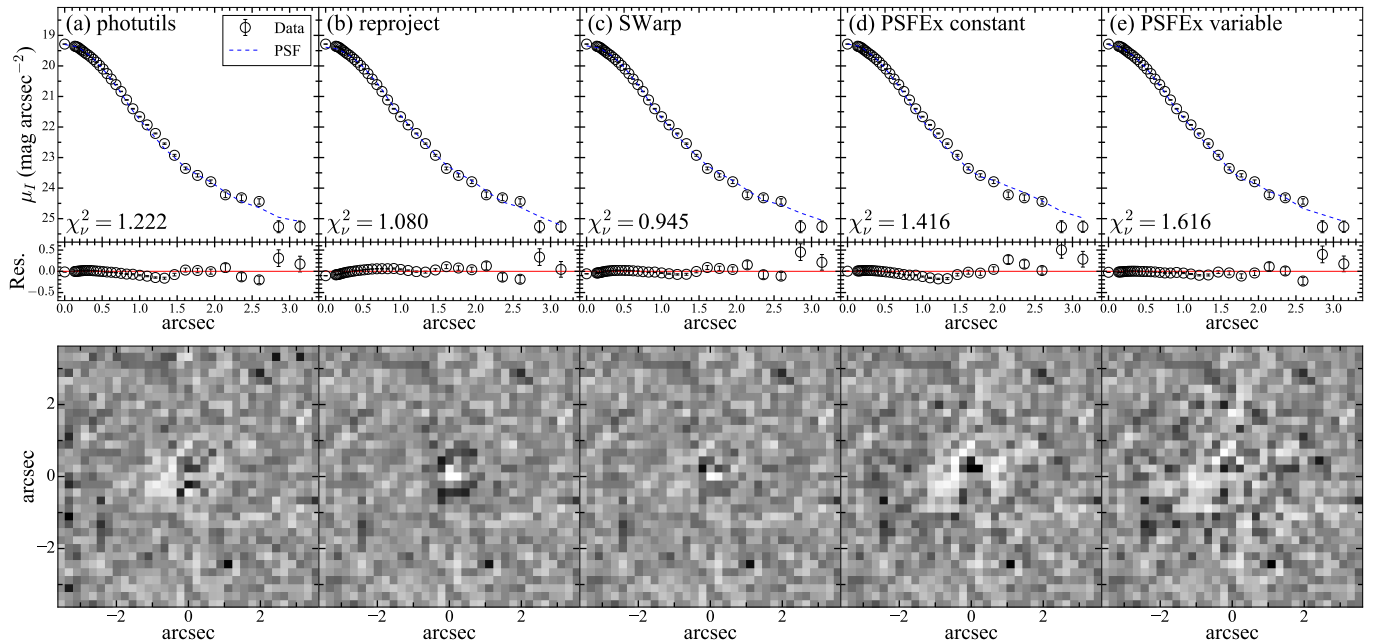


Figure 2. Top row: Surface brightness profiles of the test star (data points with error bars) shown in Figure 1 and best-fit GALFIT models of PSFs generated from different methods: (a) photutils, (b) reproject, (c) SWarp, (d) PSFEx constant, and (e) PSFEx variable. The radial profile of the residuals between the star and the PSF model is shown in the lower subpanels. Bottom row: Residual maps (data – PSF) for the different PSF models.

2. OBSERVATIONAL MATERIAL

2.1. Sample

Zhuang & Ho (2020) selected 453 AGNs with broad H α emission from the parent catalog of 14,584 low-redshift type 1 AGNs of Liu et al. (2019). They limited the sample to a narrow slice in redshift (0.3 – 0.35) to mitigate the effects of differential fiber coverage and Malmquist bias. To implement the method of SFR estimation based on the [O II] $\lambda 3727$ and [O III] $\lambda 5007$ emission lines (Ho 2005; Zhuang & Ho 2019), we additionally required the sources to have high excitation (“Seyfert” classification according to optical line-intensity ratio diagnostics; e.g., see Ho 2008), as well as narrow H α and H β lines of sufficiently high signal-to-noise ratio to yield a reliable Balmer decrement, which was used for both extinction correction and estimation of molecular gas content (Yesuf & Ho 2019). Building upon a refined [O II] SFR calibration for star-forming galaxies, Zhuang & Ho (2019) proposed, on the basis of radiation pressure-dominated photoionization models, a new SFR estimator for AGNs that explicitly accounts for the contribution of the narrow-line region to [O II], using [O III] as the benchmark for the AGN. The sample consists of powerful AGNs with bolometric luminosity $L_{\text{bol}} = 10^{44.3} - 10^{47.4} \text{ erg s}^{-1}$, BH masses $M_{\text{BH}} = 10^{6.7} - 10^{9.6} M_{\odot}$, and Eddington ratios $\lambda_{\text{E}} = 10^{-2.4} - 10^{1.6}$. The median bolometric luminosity of the sample ($L_{\text{bol}} = 10^{45.5} \text{ erg s}^{-1}$) coincides with the historical B -band absolute magnitude definition of a quasar

($M_B < -23 \text{ mag}$; Schmidt & Green 1983), upon adjusting to our adopted cosmology³.

2.2. Pan-STARRS1 3π Steradian Survey

The 3π Steradian Survey of PS1 (Chambers et al. 2016) imaged three-quarters of the sky north of declination -30° with five filters (*grizy*) and ~ 12 epochs per filter. The stacked images from this nearly four-year survey have a median seeing of $1''.31$, $1''.19$, $1''.11$, $1''.07$, and $1''.02$, and a mean 5σ point-source sensitivity of 23.3, 23.2, 23.1, 22.3, and 21.4 mag (AB) for *grizy*, respectively. The larger sky coverage, introduction of the near-infrared *y* filter, finer pixel scale ($0''.25$ versus $0''.396$), and higher sensitivity (~ 0.2 , 0.5, 0.9, 1.6 mag deeper in the *griz* bands) compared to the main SDSS photometric survey render the stacked images of the PS1 3π survey extremely valuable for studying the photometric properties of large samples of galaxies, with the possibility of even contemplating galaxies of somewhat higher redshifts. We use the stacked images, combined in each of the five bands, from the second data release (DR2; Flewelling et al. 2020) of the PS1 3π survey, which includes an improved calibration of the third full reduction of all the data (Waters et al. 2020). Each image cutout, centered on the SDSS position of the AGN, has a minimum size of $5' \times 5'$, which gradually increases in steps of $1'$ according to the

³ We convert M_B to L_{bol} using the composite quasar SED and bolometric correction at 5100 \AA from Richards et al. (2006).

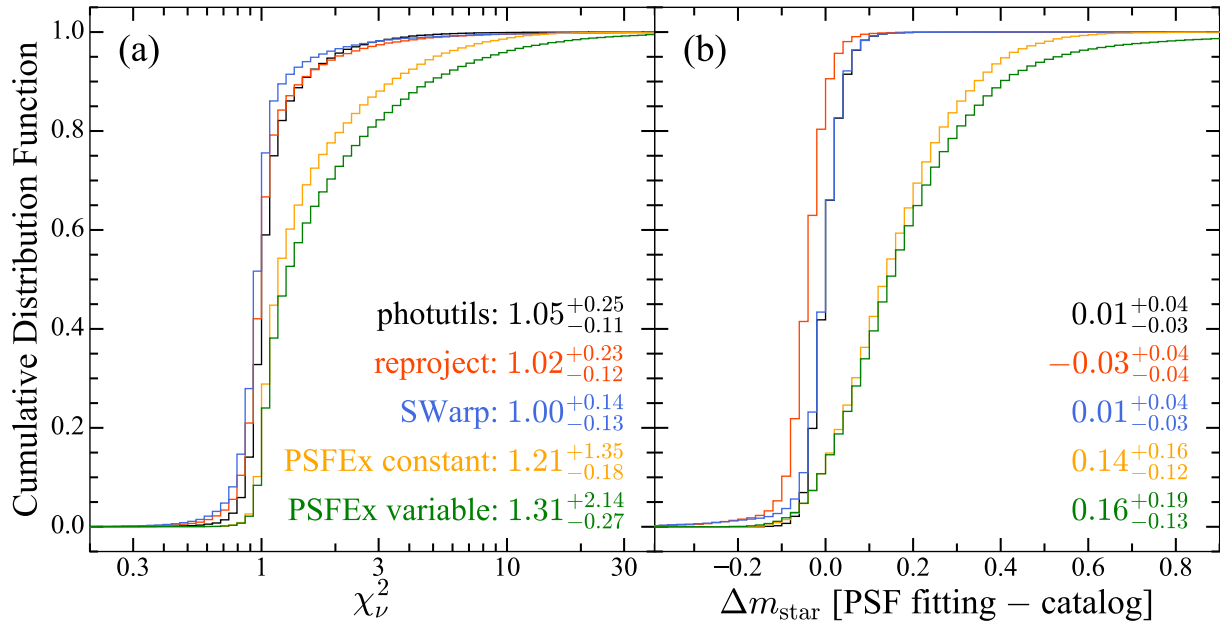


Figure 3. Cumulative distribution function of (a) χ^2_ν of the fits to test stars with PSF models using GALFIT and (b) the differences between the magnitudes of stars (m_{star}) from the PS1 DR2 catalog and those derived from PSF fitting using different PSF models. Various colors represent PSF models generated from different methods. The median and upper and lower 1σ (84th and 16th percentiles – median) values of the distributions are shown in the lower-right corner of each panel.

number of stars that are available for PSF construction and testing (Section 2.3). We also retrieve the stacked-object catalog from PS1 DR2 to obtain PSF and Kron (1980) magnitudes (m_{PSF} and m_{Kron}) for all detected objects within the field-of-view of the cutout images.

2.3. PSF Construction and Verification

To perform accurate AGN-host galaxy decomposition, obtaining an accurate PSF model is of utmost priority. We select isolated point-like sources by requiring $m_{\text{PSF}} < 21$ mag and $m_{\text{PSF}} - m_{\text{Kron}} < 0.05$ mag in the i band (Farrow et al. 2014) and removing objects with companions located within 33 pixels (~ 8 times the full width at half maximum of the PSF). At a radius of 16 pixels, light from the wings of the PSF is $\lesssim 5 \times 10^{-4}$ smaller than that of the central pixel, and thus the contamination from a companion is negligible. Choosing a larger radius would decrease the number of point sources available for PSF construction. To construct the PSF model, for each star in each band, we cut out a stamp with size 33×33 pixels after removing the background.

We consider two methods to construct the PSF model, one by building a pixel-based model and the other by stacking star images. For the pixel-based model method, we use the Python package photutils (Bradley et al. 2020) and the software PSFEx (Bertin 2011). Following the prescription of Anderson & King (2000), photutils builds an “effective” PSF that distills a representative PSF model from a set of point samplings provided by arrays of point samplings of different stars. PSFEx constructs the PSF based

on the output of SExtractor (Bertin & Arnouts 1996), using different bases generated with an algorithm similar to photutils. These include a pixel basis, which is more general and is adopted here, the Gauss-Laguerre basis, which is recommended for PSFs that are nearly Gaussian, and a user-provided vector basis. No instrument has a perfectly stable PSF that does not vary in time or position on the focal plane. PSFEx considers the spatial variation of the PSF by implementing a polynomial dependence of the PSF vector basis on position. For the image-stacking method, we use the Python package reproject⁴ and the code SWarp (Bertin et al. 2002). Three algorithms are provided to reproject images/data cubes. We use the flux-conserving scheme spherical polygon intersection, which follows the core algorithm of Montage (Berriman et al. 2008), by treating pixels as four-sided spherical polygons and computing the exact overlap of pixels on the sky. Among the several options provided by SWarp to perform reprojection, we adopt the lanczos3 routine, which is recommended as it does a good job in preserving the signal and creates relatively modest artifacts around image discontinuities.

We construct five PSF models for each object in each band, with two models from PSFEx: PSFEx constant gives a position-constant PSF, while PSFEx variable considers the spatial variation of the PSF model across the field-of-view. Considering the size of our image cutout and the

⁴ <https://reproject.readthedocs.io/en/stable/index.html>

stacking nature of the image, we adopt a second-order polynomial dependence of the PSF on pixel coordinates, which has six vectors (*constant*, x , x^2 , xy , y , and y^2 , where x and y are orthogonal pixel coordinates) and requires at least six input stars.

To obtain the best PSF model for each AGN image, we select “test stars” to evaluate the performance of the five PSF models. Test stars are point-like objects with m_{PSF} within ~ 1 mag of the target AGN. We use all point-like objects (besides the science target) in the same image cutout to construct the PSF model for the test star. Figure 1 shows an example of a test star and five corresponding PSF models constructed for it. We then use GALFIT to fit the test star with its five PSF models to obtain the goodness-of-fit χ^2_ν and best-fit magnitudes (Figure 2). For the 2265 images of the 453 objects, we use a total of 16,551 test stars (2654, 2886, 3420, 3525, and 4066 for *grizy*, respectively) and 42,093 isolated point-like sources (7949, 8803, 8240, 8739, and 8362 for *grizy*, respectively) to construct PSFs. Figure 3 gives the distribution of χ^2_ν and compares the magnitudes obtained from our PSF fitting with those from the PS1 DR2 catalog, for all test stars and five PSF models. The PSF models constructed from the different methods generally are all capable of describing the light profile of the test stars. The median value of χ^2_ν is close to 1. However, the PSF models using *photutils*, *SWarp*, and *reproject* perform significantly better than the two *PSFEX* models in recovering the magnitude of point-like sources, showing no systematic bias and a small scatter of $\lesssim 0.04$ mag. The overall good performance of the PSF models without consideration for their spatial variation suggests that this effect is not severe in the stacked images of PS1, at least for a relatively small field-of-view of ~ 30 arcmin². To assign the optimal PSF for each target, for every image of each band we select the best PSF model based on the distribution of χ^2_ν and magnitude comparisons performed using the test stars, with preference given, all else being equal, to PSF models generated using the image-stacking method. Among all 2265 images, *SWarp* and *reproject* perform best (1236 and 791 cases, respectively, or a total of $\sim 90\%$ of the sample), *photutils* stands out in 209 cases, while *PSFEX constant* and *PSFEX variable* excel compared to others in merely 24 and 5 cases, respectively.

3. IMAGE DECOMPOSITION

3.1. Two-dimensional Simultaneous Multiwavelength Fits

The morphology and structure of a galaxy may depend on wavelength as a result of internal variations in stellar population and dust attenuation. Kelvin et al. (2012) performed multi-band modeling of the images of 167,600 galaxies, fitting each galaxy independently with images covering nine filters. They find that the Sérsic index and half-light radius of both early-type and late-type galaxies vary

smoothly and systematically with wavelength: n increases and R_e decreases from the ultraviolet to the near-infrared. This reflects the fact that shorter wavelengths are more sensitive to dust attenuation and young stellar populations, while longer wavelengths better trace older stars. To account for bandpass variation of galaxy structure, we adopt GALFITM (Häußler et al. 2013; Vika et al. 2013), which can handle two-dimensional multiwavelength images under the familiar framework of GALFIT (Peng et al. 2002, 2010) by introducing a wavelength-dependent function to each galaxy model parameter. GALFITM uses a series of Chebyshev polynomials to model the wavelength dependence. The maximum order of each polynomial series can be specified by the user. All the free parameters of the model are fitted to the multi-filter data simultaneously by minimizing a single likelihood function, which significantly improves the reliability of the structural information extracted from bands with low signal-to-noise ratio (Vika et al. 2013).

We describe each active galaxy with a two-component model comprising an unresolved nucleus mimicked by the PSF and a single Sérsic function to represent the host galaxy. The fitting region is set to 51×51 pixels, which covers $\sim 60 \times 60$ kpc. As discussed in Section 3.2.1, a single Sérsic component suffices to model the stellar emission of redshift ~ 0.3 galaxies under the conditions of the PS1 survey. We follow Häußler et al. (2013) for the choice of the wavelength dependence of parameters. The ellipticity and position angle are constant with wavelength, but the magnitudes of the AGN and galaxy are free to vary with wavelength, described by a polynomial with a maximum order of 4. Häußler et al.’s analysis of $\sim 10^4$ nearby galaxies indicates that under most circumstances a linear function is enough to describe the wavelength dependence of Sérsic index n and half-light radius R_e . In a few cases, a higher second-order function is required to model the mild curvature mostly seen around the *H* band ($\sim 1.6 \mu\text{m}$). Considering the rest-frame wavelength coverage of PS1 at redshift ~ 0.3 (3600–7400 Å), we only allow n and R_e to vary linearly with wavelength. We further tie the positions of the AGN and galaxy together, as generally done in previous works (e.g., Kim et al. 2008), under the assumption that the supermassive BH is located in the center of the galaxy. Some objects have nearby companions within the fitting region. We simultaneously fit objects that are close to or overlap with our target AGN, using a PSF model for small, unresolved objects and a Sérsic model for extended, resolved sources, all the while masking other sources.

We adopt object-specific initial guesses for the position, magnitudes for the PSF model (m_{PSF}) and Sérsic model ($m_{\text{Sérsic}}$), and general parameter constraints to improve and speed up the fitting process. We take the initial guess for m_{PSF} from the PS1 catalog, which derives from fitting a PSF model alone to the object. As for the host, an initial

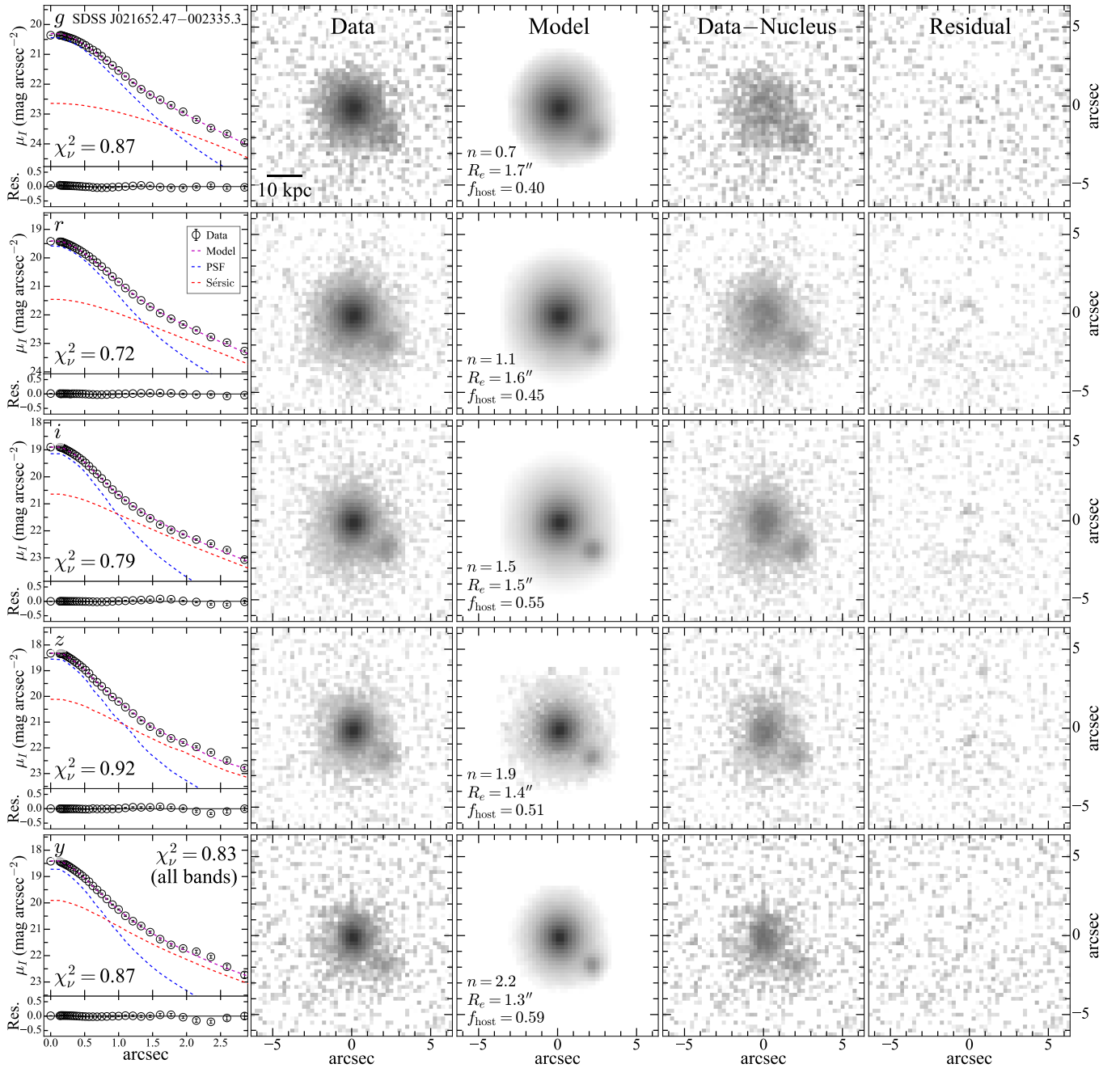


Figure 4. An example of the simultaneous multiwavelength decomposition of SDSS J021652.47-002335.3 (redshift 0.304). Rows from top to bottom are the results for filters *grizy*. The upper panel of the left column shows the radial profile of the surface brightness (open circles with error bars), PSF component (blue), Sérsic (red) component, and total model (purple; PSF + Sérsic). The χ^2_ν from GALFITM for each band is shown in the lower-left corner, while that for all five bands is shown in the upper-right corner of the first panel in the bottom row. The lower sub-panel gives the residuals between the data and the model (data-model). The images show, from left to right, the original data, best-fit total model, data with the nucleus component modeled by a PSF subtracted, and residuals of the total model. The best-fit Sérsic index, half-light radius (R_e), and host fraction $f_{\text{host}} \equiv \text{Sérsic} / (\text{PSF} + \text{Sérsic})$ are shown in the third column. Two other examples of objects with the lowest and highest χ^2_ν in the sample (see Section 4.1) are shown in Appendix A. Decomposition results of the entire sample can be found at <https://doi.org/10.12149/101130>.

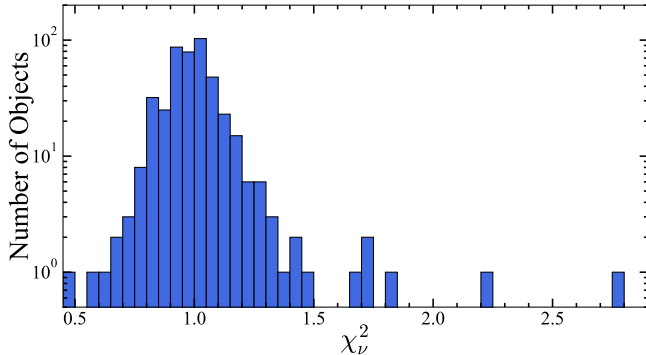


Figure 5. Distribution of χ_ν^2 of the simultaneous fits to all five bands.

guess comes from the difference between m_{Kron} and m_{PSF} , $m_{\text{Sérsic}} = -2.5 \times \log(10^{-m_{\text{Kron}}/2.5} - 10^{-m_{\text{PSF}}/2.5})$, but we constrain it to be brighter than 26 mag, ~ 4 mag weaker than the faintest detected object. The Sérsic index is allowed to vary within the range $n = 0.3 - 8$ and the half-light radius $R_e = 0.5 - 20$ pixels, which corresponds to $\sim 0.6 - 22.3$ kpc at redshift 0.3. In practice, these boundaries are seldom reached during the fitting process.

An example of our simultaneous, multi-object, multi-band decomposition is given in Figure 4. The smooth residuals and low χ_ν^2 indicate that the fitting is quite successful. From the surface brightness profiles, we can clearly discern the extended emission from the host galaxy and distinguish it from the unresolved nucleus. Consistent with our expectations, we find that the host-to-total flux ratio ($f_{\text{host}} = 0.40 - 0.59$) and Sérsic index ($n = 0.7 - 2.2$) increase significantly and systematically from the g band to the y band. Note that at redshift ~ 0.3 broad H α falls into the z bandpass, causing f_{host} to decrease from 0.55 in the i band to 0.51 in the z band.

For most of the objects, we achieve good fits overall with χ_ν^2 peaked at ~ 1 (Figure 5). Six outliers ($\chi_\nu^2 > 1.5$) have significant residuals and are excluded from further analysis. Two additional objects are removed because they suffer from contamination by a nearby, bright star.

3.2. Verification of Results

The rich morphological complexities of galaxies are difficult to describe by simplified parametric models. Parameters returned by codes such as GALFIT and GALFITM may suffer from various degrees of systematic bias and degeneracy, which will result in underestimation of the true uncertainties, even if the formal statistical errors are small and the fitting residuals look acceptable (e.g., Häussler et al. 2007; Kim et al. 2008; Vika et al. 2013; Gao & Ho 2017; Zhao et al. 2021). We design realistic input-output experiments to verify our results using two sets of mock AGNs: one from galaxies actually observed at redshift ~ 0.3 and another from model galaxies generated from best-fit parameters.

3.2.1. Mock AGNs from Real Galaxies

Even though a single Sérsic function can describe the overall emission profiles of AGN host galaxies at redshift ~ 0.3 as observed under the conditions of PS1 (Figures 4 and 5), significant uncertainties can arise from model mismatch, as the assumed model vastly oversimplifies the true underlying galaxy, which can contain substructures such as rings, lenses, bars, and spiral arms. To investigate whether and to what extent our results are affected by these potential issues, we generate mock AGNs by adding an artificial point source to the center of real redshift ~ 0.3 galaxies, and then compare the parameters measured before and after the addition of the point source.

For this purpose, we select objects with spectroscopic redshifts from the zCOSMOS survey (Lilly et al. 2009) in the COSMOS field (Scoville et al. 2007), which is covered in the PS1 survey footprint. These objects have abundant information, such as high-resolution images from the HST Advanced Camera for Surveys (ACS) (Koekemoer et al. 2007), multiwavelength data from the X-rays to the radio, morphological classifications (Scarlata et al. 2007), and stellar mass measurements (Laigle et al. 2016). We choose 111 redshift 0.30 – 0.35 galaxies with morphological classification and $M_* = 10^{10.4} - 10^{11.4} M_\odot$, which spans the 5th–95th percentile of the stellar mass range of our quasars, taking care to avoid objects close to bright stars. To ensure that these are genuine representations of inactive galaxies, we exclude objects with detected X-ray emission.

Since the image-stacking method provides overall better performance than the pixel-basis method (Section 2.3), we only use `reproject` to construct the PSF models. We then use GALFITM to perform multiwavelength simultaneous fitting to derive the parameters of the redshift ~ 0.3 galaxies, following the same procedure as that employed for the AGNs. Figure 6 gives examples of high-resolution HST ACS/F814W images, PS1 i -band images, best-fit models, and residual images for galaxies of three different morphologies (early-type, bulge-dominated, and disk-dominated). The residuals are quite clean. This exercise demonstrates that a single Sérsic component adequately describes the galaxy light distribution at redshift ~ 0.3 , for images of galaxies that should closely resemble those of the underlying population of AGN hosts under consideration, as captured with the image quality and observational characteristics of PS1.

To generate mock active galaxies, we add a point source to the center of each galaxy with AGN strength following the same distribution as the actual AGN sample. From the catalog of Liu et al. (2019), for our sample the 5th, 16th, 50th, 84th, and 95th percentile of the monochromatic AGN continuum luminosity at 5100 Å is $\log(L_{5100}/\text{erg s}^{-1}) = 43.7, 43.9, 44.2, 44.5, \text{ and } 44.8$, respectively. With the composite quasar SED of Richards et al. (2006), at a median

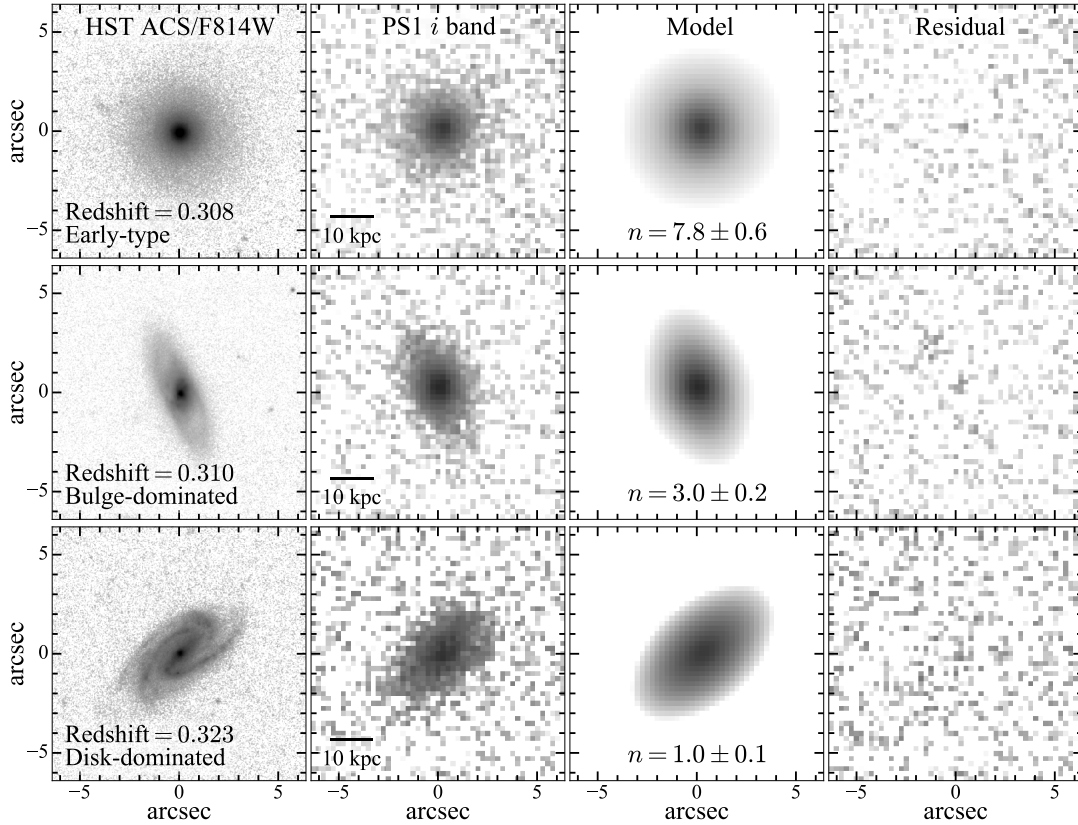


Figure 6. Examples of images and fits using GALFITM for (top) early-type, (middle) bulge-dominated, and (bottom) disk-dominated galaxies. The columns, from left to right, show the HST ACS/F814W image, the PS1 i band image, the best-fit single Sérsic model for the i band, and the residuals (data – model). The best-fit Sérsic index n and its uncertainty are shown in the panel for the model.

redshift of 0.32 these values of L_{5100} translate to $m_{\text{AGN}} = 19.9, 19.6, 18.9, 18.0,$ and 17.4 mag for the i band. In the end, we have in total 555 mock AGNs spanning the same parameter space as our true sample. Examples of fits of mock AGNs with different m_{AGN} are shown in Figure 7. For the brightest case ($m_{\text{AGN}} = 17.4$ mag), the nucleus can dominate the observed total emission even out to a radius of $\sim 3''$. Fortunately, even under these conditions the AGN point source can still be distinguished from the extended emission of the underlying host galaxy.

To test whether we can reliably recover the host galaxy parameters in the presence of an AGN, we compare $m_{\text{Sérsic}}$ before and after adding a simulated active nucleus to the galaxy image (Figure 8). In general, $m_{\text{Sérsic}}$ can be recovered with quite good consistency in $rizy$, with a small median magnitude difference ($\lesssim 0.1$ mag) and ~ 0.2 mag scatter within the 16th and 84th percentiles of the range of AGN strengths explored (three middle rows). The higher contrast between the AGN and its host galaxy in the g band introduces a larger systematic difference (0.09 mag) and scatter (~ 0.3 mag; averaged over the 16th, 50th, and 84th percentiles of AGN strength). At the same time, the fraction of objects with measurement values less than 3 times its error (unreliable mea-

surements) is much higher compared to the average of the other four bands (39% versus 21%). The best performance is found in i , for which the fraction of unreliable measurements is only 13.5%. Even in the extreme case when the AGN strength is at the 95th percentile, we still achieve reasonable consistency in the $rizy$ bands, with the g band, once again, faring the worst.

Figure 9 examines the effect of the AGN on our ability to measure the Sérsic index and half-light radius, focusing on the results in the i band, which gives the best performance. We find that the presence of an AGN generally leads to a systematic underestimate of n , on average by ~ 0.08 dex. The effect of PSF convolution evidently reassigns a portion of the central galaxy flux to the point source, which lowers the value of n . The parameter least affected is R_e , with close to zero systematic offset and only ~ 0.12 dex scatter between the 16th and 84th percentiles of AGN strength.

We also assess the performance of separate single-band decomposition, as commonly practiced in previous works (e.g., Matsuoka et al. 2014; Ishino et al. 2020; Li et al. 2021a). With the same set of mock AGNs generated here, we fix the galaxy structure to that determined from the i band and compare the behavior of separate single-band decomposition

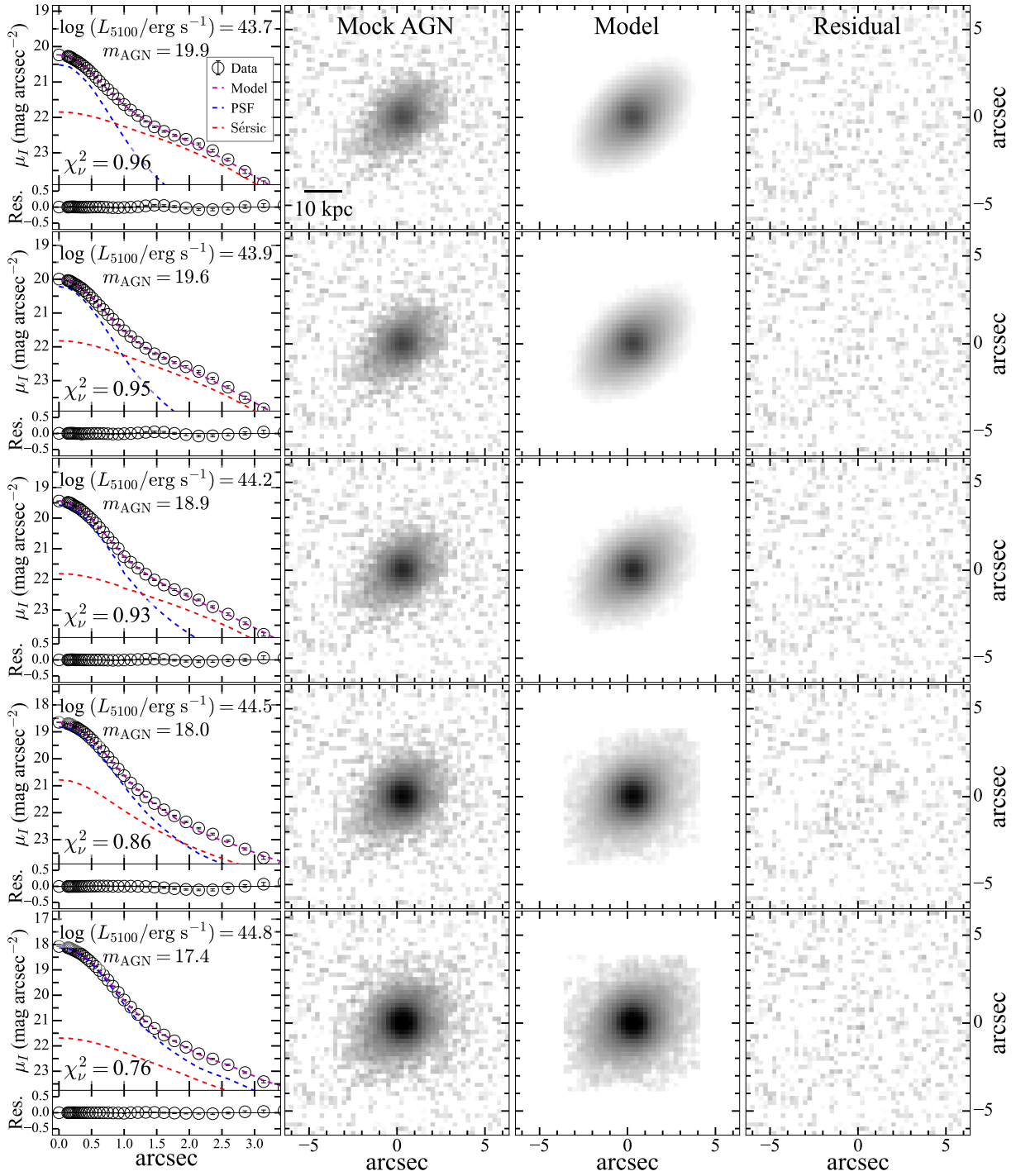


Figure 7. Examples of fits to mock AGNs in the i band generated from the third (disk-dominated) object in Figure 6 ($m_{\text{Sérsic}} = 19.1$ mag) with AGN strength increasing from $m_{\text{AGN}} = 19.9$ mag (top) to 17.4 mag (bottom). Columns are similar to Figure 4, showing the surface brightness profile, data of the mock AGN, the best-fit model, and the residuals (mock AGN – model).

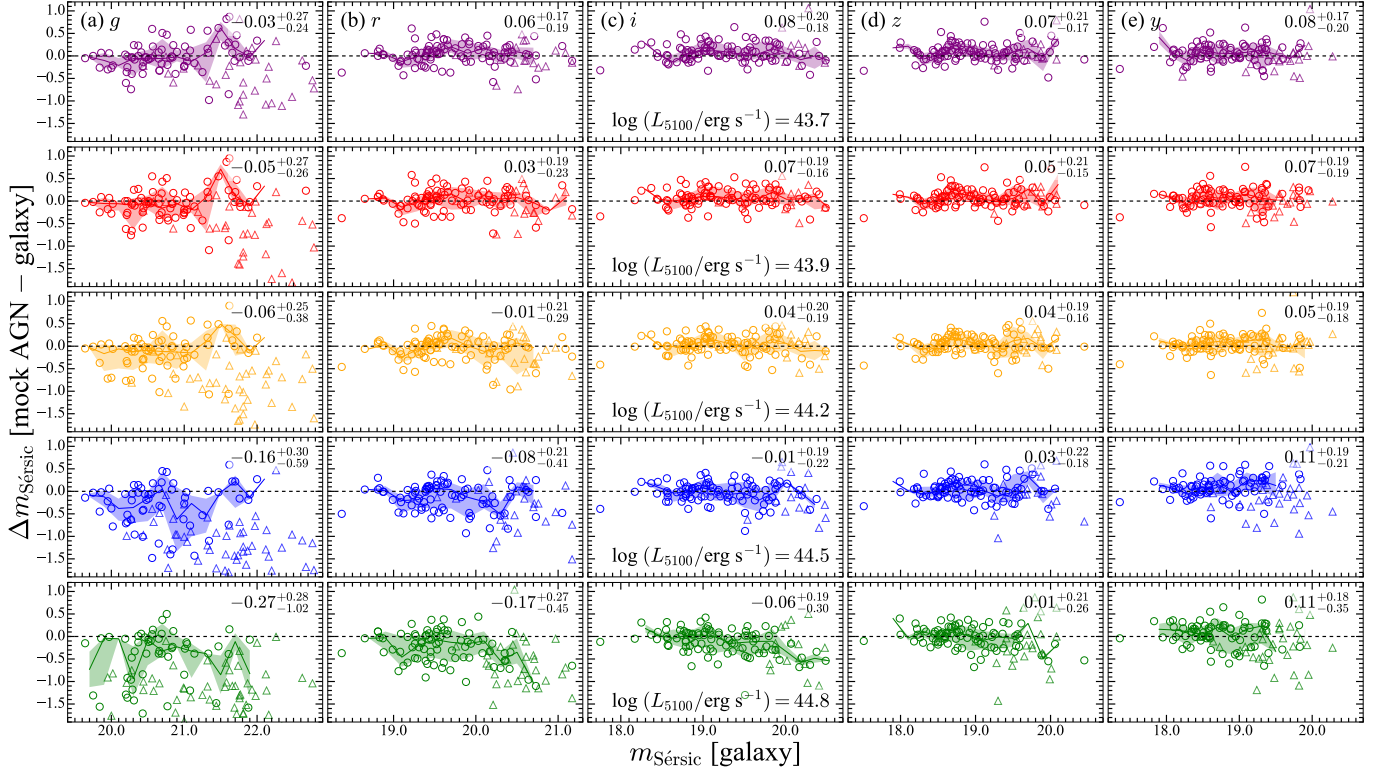


Figure 8. Comparison of the difference in $m_{\text{Sérsic}}$ ($\Delta m_{\text{Sérsic}}$) between the best-fit magnitude measured before and after adding the mock AGN, for galaxies selected from the COSMOS field as observed in the *grizy* bands (panels a–e). Various colors represent AGNs with different strengths (L_{5100}), ranging from the 5th (purple), 16th (red), 50th (orange), 84th (blue), and 95th (green) percentiles of our redshift = 0.3 quasar sample. Circles represent objects with value at least 3 times its error, and faint triangles are for those with value less than 3 times its error. The upper-right corner of each panel gives the median and upper and lower 1σ (84th and 16th percentiles – median) of $\Delta m_{\text{Sérsic}}$ of the circles.

with our preferred method of simultaneous multiwavelength decomposition. The performance is notably inferior, as summarized in Appendix B.

Our mock tests attempt to simulate, to the extent possible, conditions that resemble our actual observed sample. We demonstrate that we can obtain reliable estimates of host galaxy magnitude and size. Significant scatter remains, however, and the systematic uncertainties on Sérsic index are particularly serious, as are difficulties with the *g* band where AGN contamination becomes most acute, or in the *y* band where the sensitivity sharply drops. We apply systematic corrections to n and $m_{\text{Sérsic}}$ (the latter only in the *g* and *y* bands) based on the mean offsets from the true values measured at the 16th, 50th, and 84th percentiles of AGN strength, and we include the corresponding mean scatter into the error budget as a quadrature sum. A summary of the uncertainties is given in Table A1 of Appendix B. As expected, stronger AGNs in images of lower signal-to-noise (shorter exposure time) may completely dominate the observed fluxes due to high sky background level and lead to unreliable results. To help mitigate against this issue, we use SED fitting to help rule out objects with unrealistic SEDs (see Section 4.1).

3.2.2. Mock AGNs from Idealized Galaxies

The above simulations neglect the complication that the PS1 images do not have uniform depth. The exposure times of our sample range from a minimum of 390 s to a maximum of 3720 s, with a median of 817, 896, 1427, 720, and 800 s in the *grizy* bands, respectively. For reference, the median exposure times for the matched galaxy sample in the COSMOS field discussed in Section 3.2.1 are longer in *gr* and shorter in *izy*. This difference makes it difficult to assess the impact of signal-to-noise ratio on individual objects. We address this issue using idealized simulations in which we use the best-fit parameters derived for each object to construct mock images that exactly mimic the object-specific parameters of the actual observation. For each object in each band, we generate 100 realizations of mock observations that account for the Poisson noise associated with the source, background Gaussian noise, and the properties of the specific image (gain, exposure time, and background variation). Then, we use GALFITM to repeat the decomposition and adopt the median value and standard deviation of the 100 results as the measurement and its error. Excellent consistency is found with the input values (Figures 10 and 11), with no detectable systematic bias and very small scatter. A handful of objects (highlighted with crosses) deviate by more than 3 times its uncertainty. We exclude the objects with inconsistent fluxes

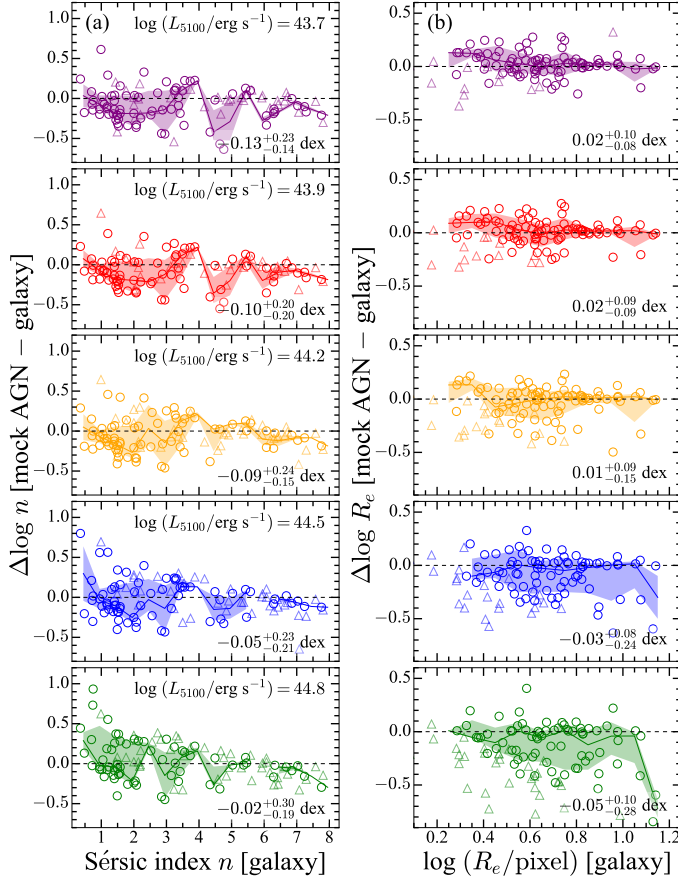


Figure 9. Same as in Figure 8, but for (a) Sérsic index n and (b) half-light radius R_e . We focus only on the results for the i band. The statistics in panel (a) are calculated after taking the logarithm of the value (i.e., $\log n$).

when analyzing the SEDs in Section 4.1, and those with highly discrepant n or R_e are deemed to have unreliable morphology in Section 4.2. The uncertainties derived from this set of simulations are added in quadrature to the final error budget of each parameter.

4. RESULTS

4.1. Derivation of Stellar Masses

We use the SED fitting code CIGALE (Boquien et al. 2019) to derive the stellar masses of the host galaxies. We first correct the photometry for Galactic foreground extinction using the Python package dustmaps (Green 2018) and the dust maps from Schlegel et al. (1998), converting $E(B - V)$ to extinction for the PS1 bands assuming $R_V = 3.1$ (Schlafly & Finkbeiner 2011). We only consider objects with host galaxy component detected in at least four bands with a signal-to-noise ratio of 3. This reduces the sample to 366 objects (332 detected in all five bands, 34 detected in four bands), or 81% of the original sample. Most of the non-detections are in the g band, mostly attributable to non-uniform exposure time, in-

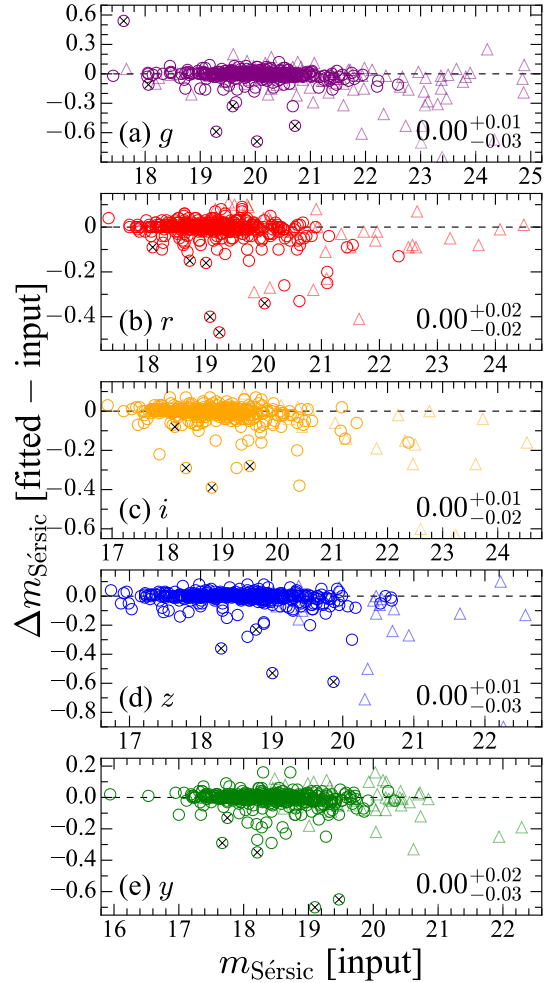


Figure 10. Comparison of best-fit $m_{\text{Sérsic}}$ of the mock AGNs with those used as input parameters to generate mock AGNs in the five bands (panels a–e). Mock AGNs are generated using best-fit parameters from simultaneous fitting to observed five-band data for the real AGNs. Symbols are the same as in Figure 8. Objects with $|\Delta m_{\text{Sérsic}}| > 3\delta m_{\text{Sérsic}}$ are marked with crosses, where $\delta m_{\text{Sérsic}}$ is the error of $m_{\text{Sérsic}}$. The median and upper and lower 1σ (84th and 16th percentiles – median) of the differences (fitted – input) for the detections (circles excluding crosses) are shown in the lower-right corner of each panel.

trinsic weakness of the galaxy, or high AGN-to-host contrast in the blue.

We adopt a “delayed” star formation history model, which has a functional form $\text{SFR}(t) \propto t/\tau^2 \exp(-t/\tau)$, with τ the e-folding time of the stellar population, and an exponential burst to allow for a recent episode of star formation (e.g., Kauffmann et al. 2003; Wild et al. 2007; Kim & Ho 2019). The stellar component is represented using single stellar population models from Bruzual & Charlot (2003, BC03), with a Chabrier (2003) initial mass function and solar metallicity (0.02). Stellar masses are converted to our adopted Kroupa (2001) initial mass function by multiply-

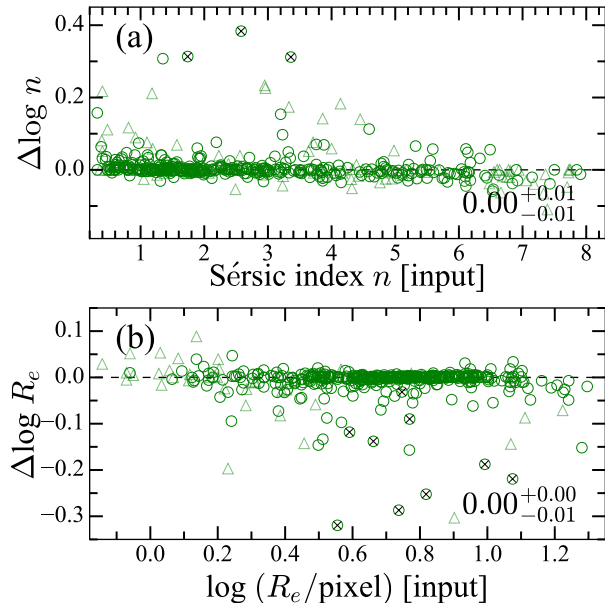


Figure 11. Similar as Figure 10, but for (a) Sérsic index n and (b) half-light radius R_e . We focus only on the results for the i band.

ing by a factor of 1.08 (Madau & Dickinson 2014). We assume a fixed ionization parameter ($\log U = -2$) for the nebular emission. Both the stellar continuum and the nebular emission are attenuated by dust using the `dustatt` modified starburst module, assuming the extinction law of Calzetti et al. (2000) and a fixed ratio of 0.44 for the $E(B - V)$ of the stellar continuum to that of the line emission. The modules and input parameters used in this paper are given in Table 1. Figure 12 shows an example SED fit to the five-band PS1 photometry.

We obtain the stellar mass from a Bayesian estimate provided by `CIGALE`, which is based on the probability density function of the likelihood associated with every template. Since our error is likely overestimated due to the statistical correction applied in Section 3.2 from analysis of mock AGNs, we only limit our attention to objects with high-quality SED fits ($\chi^2_\nu \leq 1$). Incorporating an additional burst component has a negligible impact on the majority of the derived stellar masses (0.02 ± 0.03 dex; Figure 13a), and for the sake of reducing the number of free parameters, we adopt the star formation history model without a burst component. A minority of the sample (34 objects) have incomplete SEDs, missing data in one of the bands. We evaluate the significance of the gap in SED coverage by artificially removing a single band from the objects having complete SEDs. The g and y bands are affected the most (scatter 0.10 and 0.08 dex, respectively), but in general the effects are minimal, with median systematic differences of $|\Delta \log M_*| \leq 0.02$ dex for all four bands (Figure 13b). We add the corresponding uncer-

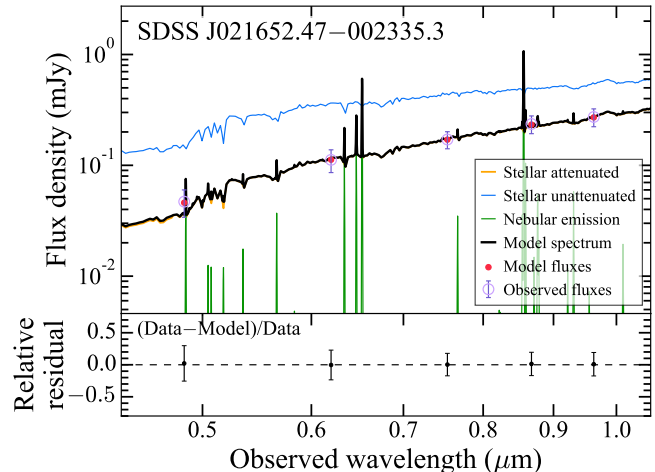


Figure 12. SED fitting to the five PS1 bands of SDSS J021652.47–002335.3 using `CIGALE`. The observed fluxes (purple open circles) have been subtracted of AGN contribution. The upper panel shows the best-fit total model spectrum (black solid curve), its components (stellar attenuated: yellow solid curve; nebular emission: green solid curve), the model fluxes (red filled circles), and the stellar emission before attenuation (blue curve). Relative residuals (data–model)/data are shown in the lower panel.

tainty into the error budget for the stellar masses of the objects lacking photometry in the g or y band.

Finally, we successfully obtained reasonably accurate stellar masses for 305 of the 366 ($\sim 84\%$) objects with good fits ($\chi^2_\nu \leq 1$). The median uncertainty of the stellar mass is 0.2 dex. This final sample, which has a similar distribution of redshift and AGN bolometric luminosity as the parent sample (Figure 14), is by far the largest sample of quasars with derived stellar masses at redshift ~ 0.3 . We present the basic properties of the final sample in Table 2. Table 3 gives the fluxes of the host galaxies in the five PS1 bands, along with derived physical properties.

4.2. Estimation of Host Galaxy Morphologies

Well-resolved images are required for rigorous morphological classification of galaxies, be they nearby (e.g., Gao et al. 2019) or distant (e.g., van der Wel et al. 2012; Davari et al. 2017). At redshifts ~ 0.3 , the arcsecond-scale resolution of the PS1 images subtends a physical scale of ~ 2.3 kpc in radius, which is inadequate for reliable bulge-to-disk decomposition. The presence of a bright nucleus doubly exacerbates the situation. As a consequence, we have confined

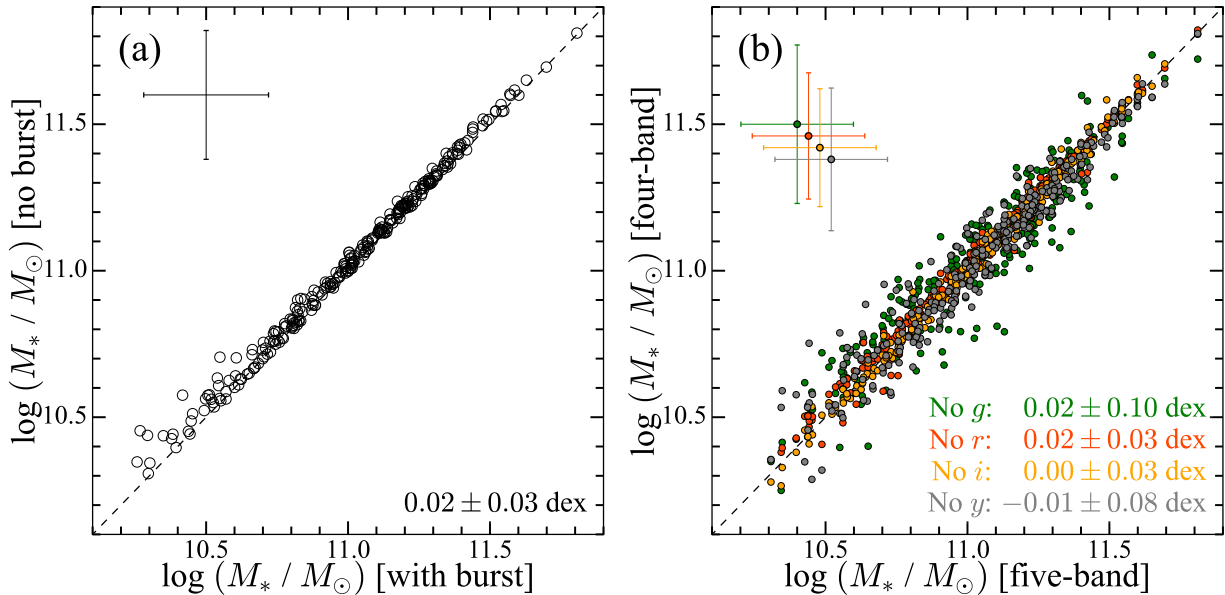


Figure 13. Comparison of stellar masses for 286 objects with $\chi^2_{\nu} \leq 1$ derived from CIGALE (a) with and without including a burst component in the star formation history model and (b) using complete (five-band) and incomplete (four-band) photometry after manually removing one of the bands. The green, red, orange, and gray dots represent objects with the g , r , i , or y band removed, respectively. Median differences (y-axis – x-axis) and standard deviations for each comparison are shown in the lower-right corner; typical uncertainties are shown in the upper-left corner. The dashed line gives the 1:1 relation.

Table 1. Parameters of the SED Fits

Model	Parameter	Value
Star formation history: delayed	e-folding time of the main stellar population in Gyr (τ_{main})	0.001, 0.1, 0.25, 0.5, 0.75, 1.0, 1.5, 2.0, 2.5, 3.0, 4.0, 5.0, 6.0, 8.0, 10, 12, 15, 20
	Age of the main stellar population in Gyr (age_{main})	9.0
	e-folding time of the late starburst population in Myr (τ_{burst})	5, 10, 25, 50, 100, 250, 500, 750, 1000
	Age of the late burst in Myr ($\text{age}_{\text{burst}}$)	10, 25, 50, 100, 200, 250, 500, 750, 1000
	Mass fraction of the late burst population (f_{burst})*	-10^{-5} , 0, 0.005, 0.01, 0.015, 0.02, 0.04, 0.07, 0.10, 0.15, 0.20, 0.30
Single stellar population:	Initial mass function	Chabrier
BC03	Metallicity	0.02 (solar)
Nebular emission	Ionization parameter ($\log U$)	-2.0
Dust attenuation: modified starburst attenuation law	The color excess of the nebular lines in mag [$E(B - V)$]	0.0, 0.001, 0.005, 0.01, 0.03, 0.05, 0.1, 0.2, 0.3, 0.4, 0.5, 0.6, 0.8
	Ratio of $E(B - V)$ between stellar continuum and emission line	0.44

NOTE—*A very small negative value is used to increase the parameter sampling close to 0.

our image decomposition to the simplest single-component model to fit the host galaxy. Fortunately, the galaxies in the COSMOS field have detailed morphological classifications based on high-resolution HST ACS/F814W images from the Zurich Estimator of Structural Type (ZEST) catalog (Scarlata et al. 2007). ZEST classified galaxies into three structural types (early-type, disk, and irregular galaxies) using a

three-dimensional space defined by the three main eigenvectors from a principal component analysis of five nonparametric quantities. With a more detailed subtype (“bulgeness”) for disk galaxies refined using the help of the source’s Sérsic index, which is loosely correlated with the bulge-to-disk ratio, the catalog distinguishes the disk galaxies into more detailed subtypes (bulge-dominated disk, intermediate-bulge

Table 2. Basic Properties of the Final Sample

Index	Name	Redshift	R. A.	Dec.	$\log M_{\text{BH}}$	$\log L_{\text{bol}}$	$\log \dot{M}_{\text{BH}}$	$\log \lambda_{\text{E}}$	$\log \text{SFR}$
(1)	(2)	(3)	($^{\circ}$)	($^{\circ}$)	(M_{\odot})	(erg s^{-1})	($M_{\odot} \text{ yr}^{-1}$)	(9)	($M_{\odot} \text{ yr}^{-1}$)
(1)	(2)	(3)	(4)	(5)	(6)	(7)	(8)	(9)	(10)
1	SDSS J002822.54−103903.5	0.301712	7.0939008	−10.650981	7.85	44.92 ± 0.15	$−0.9 \pm 0.15$	−1.03	0.73 ± 0.18
2	SDSS J003321.77+141626.5	0.300153	8.340729	14.274034	7.50	44.94 ± 0.25	$−0.89 \pm 0.25$	−0.66	1.13 ± 0.36
3	SDSS J004214.71+153148.2	0.316244	10.56129	15.530053	7.51	45.11 ± 0.24	$−0.72 \pm 0.24$	−0.50	1.23 ± 0.33
4	SDSS J004319.75+005115.3	0.308341	10.832272	0.85425062	9.55	45.41 ± 0.16	$−0.41 \pm 0.16$	−2.24	1.03 ± 0.21
5	SDSS J004458.67+004319.9	0.349953	11.244478	0.72219575	8.13	45.38 ± 0.16	$−0.44 \pm 0.16$	−0.85	0.62 ± 0.30
6	SDSS J012256.19−000252.6	0.340495	20.734137	−0.04794548	7.96	45.66 ± 0.18	$−0.16 \pm 0.18$	−0.40	1.54 ± 0.24
7	SDSS J013352.65+011345.4	0.308083	23.469391	1.2292659	8.31	45.27 ± 0.16	$−0.56 \pm 0.16$	−1.14	0.14 ± 0.55
8	SDSS J015957.64+003310.5	0.311674	29.990148	0.55291729	8.00	44.81 ± 0.14	$−1.01 \pm 0.14$	−1.29	1.01 ± 0.12
9	SDSS J021652.47−002335.3	0.304493	34.21864	−0.39314734	7.25	45.72 ± 0.20	$−0.1 \pm 0.20$	0.37	1.57 ± 0.28
10	SDSS J022138.74+005048.3	0.306465	35.411399	0.8467546	7.66	44.93 ± 0.18	$−0.9 \pm 0.18$	−0.83	0.87 ± 0.23

NOTE—Col. (1): Object index. Col. (2): Object name. Col. (3): Right ascension (J2000). Col. (4): Declination (J2000). Col. (5): Redshift. Col. (6): BH mass estimated using broad H α from Liu et al. (2019). We adopt a conservative uncertainty of 0.5 dex following Kim & Ho (2019). Col. (7): AGN bolometric luminosity. Col. (8): BH accretion rate. Col. (9): Eddington ratio, whose uncertainty is dominated by the uncertainty of M_{BH} . Col. (10): Star formation rate. Cols. (7)–(10) are from Zhuang & Ho (2020). (Table 2 is published in its entirety in the machine-readable format.)

Table 3. Fluxes and Derived Properties of the Final Sample

Index	f_g	f_r	f_i	f_z	f_y	$\log M_{\star}$	n	R_e	Morphology
(1)	(mJy)	(mJy)	(mJy)	(mJy)	(mJy)	(M_{\odot})	(8)	(kpc)	(10)
(1)	(2)	(3)	(4)	(5)	(6)	(7)	(8)	(9)	(10)
1	0.049 ± 0.014	0.112 ± 0.026	0.166 ± 0.029	0.207 ± 0.037	0.231 ± 0.042	11.06 ± 0.20	1.71 ± 0.70	5.99 ± 1.67	late
2	0.036 ± 0.011	0.087 ± 0.020	0.160 ± 0.028	0.201 ± 0.037	0.184 ± 0.036	11.09 ± 0.18	2.19 ± 0.90	4.72 ± 1.31	early
3	0.034 ± 0.014	0.077 ± 0.024	0.092 ± 0.020	0.161 ± 0.038	0.089 ± 0.033	10.67 ± 0.26	...	7.29 ± 2.30	uncertain
4	0.058 ± 0.023	...	0.221 ± 0.046	0.334 ± 0.072	0.308 ± 0.084	11.33 ± 0.24	7.36 ± 3.38	9.77 ± 3.15	early
5	0.058 ± 0.017	0.132 ± 0.031	0.164 ± 0.030	0.211 ± 0.039	0.189 ± 0.039	10.97 ± 0.20	3.52 ± 1.47	5.62 ± 1.57	early
6	0.043 ± 0.016	0.086 ± 0.024	0.128 ± 0.026	0.126 ± 0.030	0.113 ± 0.039	10.77 ± 0.24	5.73 ± 2.49	2.83 ± 0.85	early
7	0.075 ± 0.023	0.119 ± 0.029	0.203 ± 0.039	0.398 ± 0.076	0.437 ± 0.088	11.46 ± 0.24	6.26 ± 2.66	10.11 ± 2.96	early
8	0.034 ± 0.012	0.109 ± 0.028	0.128 ± 0.027	0.163 ± 0.045	0.151 ± 0.060	10.96 ± 0.25	4.97 ± 2.19	1.75 ± 0.58	early
9	0.047 ± 0.013	0.112 ± 0.026	0.171 ± 0.030	0.236 ± 0.043	0.273 ± 0.050	11.20 ± 0.18	1.85 ± 0.77	6.64 ± 1.86	late
10	0.037 ± 0.011	0.101 ± 0.024	0.160 ± 0.029	0.219 ± 0.040	0.310 ± 0.057	11.31 ± 0.18	3.07 ± 1.27	6.52 ± 1.82	early

NOTE—Col. (1): Object index. Cols. (2)–(6): Flux density of AGN host galaxy in the *grizy* bands after correction for Galactic extinction and systematic effects (Section 3.2). Col. (7): Stellar mass from SED fitting. Cols. (8)–(9): Sérsic index n and half-light radius in the *i* band after correction for systematic effects (Section 3.2). Col. (10): Morphological classification based on n and R_e . (Table 3 is published in its entirety in the machine-readable format.)

disk, and pure disk). To evaluate the feasibility of estimating morphological types from our data, we take advantage of the available classifications from ZEST, in conjunction with the i -band Sérsic indices and half-light radii measured from simultaneous multiwavelength fits of the PS1 images of a subset of redshift ~ 0.3 galaxies in the COSMOS field. For this work, we only define two broad bins of morphological types: (1) early-type, which includes galaxies classified by ZEST as ellipticals, spheroidals, and bulge-dominated disk galaxies, and (2) late-type, which combines all other sources classified by ZEST as disk galaxies, including intermediate-bulge disk galaxies and pure disk galaxies. Figure 15 shows that late-type galaxies preferentially have smaller n and larger R_e . A combination of a horizontal line with $n \leq 2$ and a vertical line with $R_e \geq 2$ kpc approximately separates the two galaxy types, with a false positive (misclassification) rate of $\sim 24\%$ for early-type and 22% for late-type galaxies. A few outliers with high n ($\gtrsim 4$) and small R_e ($\lesssim 5$ kpc) are classified as late-type galaxies according to ZEST. Visual inspection of their HST images, however, reveals that these galaxies indeed have a prominent bulge component besides a disk, and they should be better described as early-type. Therefore, the actual false positive rates may be somewhat more favorable than the above statistics indicate. We note that 4/111 objects are classified as irregular by ZEST. Of these, two exhibit features that may be associated with interactions. The combination of n and R_e still gives a reasonable estimate of their morphologies (three late-type and 1 early-type systems).

Bearing in mind the obvious limitations of our crude method and the large uncertainty of the individual values of n , we apply our empirical classification scheme to estimate the host galaxy morphology of our quasar sample (Table 3). Among 305 quasars, 9 (3%) have highly uncertain n or/and R_e based on the mock tests using idealized galaxies in Section 3.2.2, and we label their morphologies as “unreliable.” For the remaining 296 quasars (97% of the total sample), 175 (57%) reside in early-type galaxies and 121 (40%) are hosted by late-type galaxies, consistent with the significant late-type fraction found in previous studies of low-redshift, optically selected type 1 quasars (e.g., Falomo et al. 2014; Kim et al. 2017; Yue et al. 2018; Li et al. 2021a; Zhao et al. 2021), optically selected type 2 quasars (Zhao et al. 2019), and X-ray-select AGNs (e.g., Gabor et al. 2009; Kim et al. 2021).

4.3. Mass-size Relation

The stellar mass of a galaxy and how that mass is distributed spatially, commonly described by the stellar mass-size relation, encode vital clues about the galaxy’s evolution and assembly history. The mass-size relation differs between galaxies of early and late type, and it evolves strongly with redshift (see, e.g., review in Somerville & Davé 2015). Fig-

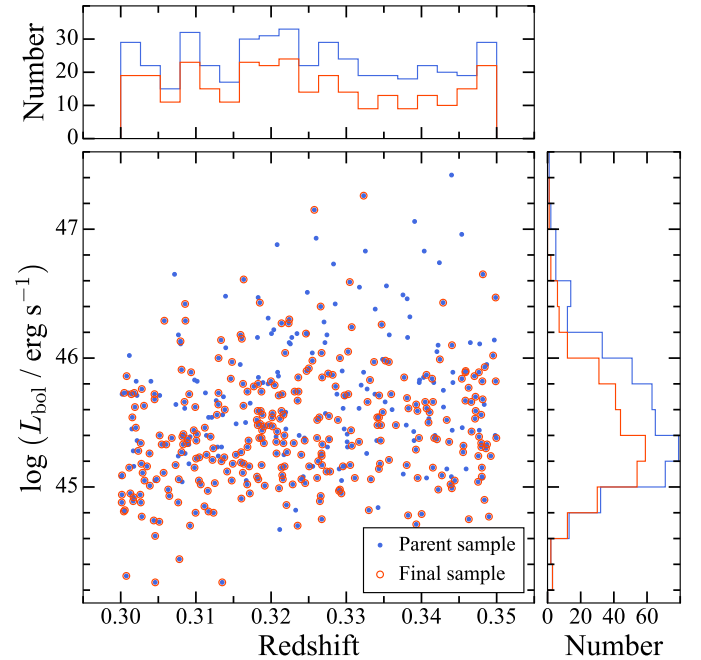


Figure 14. Comparison of redshifts and AGN bolometric luminosities (L_{bol}) for the parent sample (453 objects) and final sample (305 objects) that has CIGALE fits with $\chi^2_{\nu} \leq 1$.

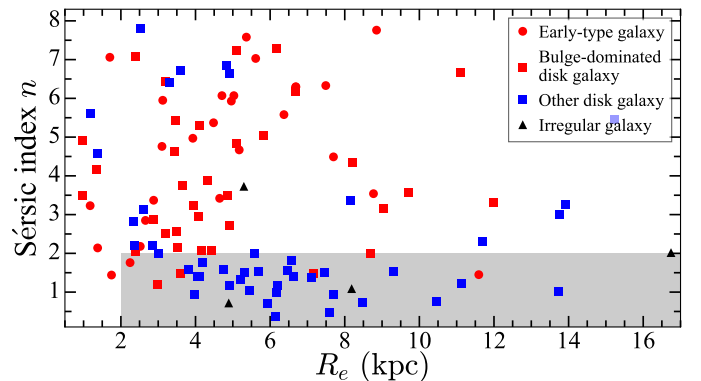


Figure 15. Distribution of Sérsic index (n) versus effective radius (R_e) measured in the PS1 i band for redshift ~ 0.3 galaxies selected from the COSMOS field (Section 3.2.1). Morphological type information is from the Zurich Estimator of Structural Type (ZEST) catalog (Scarlata et al. 2007), which is based on high-resolution HST images. Circles, squares, and triangles represent early-type, disk, and irregular galaxies, respectively, as given in the ZEST catalog. Red and blue symbols are early-type and late-type galaxies according to our definition; the shaded area denotes the region dominated by late-type galaxies.

ure 16 illustrates that the early-type and late-type host galaxies of red quasars follow the same $M_* - R_e$ relations defined by the inactive galaxy population at a similar redshift (0.25;

van der Wel et al. 2014)⁵. As with the regular galaxy population, at the same M_* early-type galaxies are systematically more compact (smaller R_e) than late-type galaxies. Closer inspection reveals something more: $\sim 1/3$ (107/305) of the quasars lie below the $M_* - R_e$ relation of either galaxy type by at least 1σ (the blue and red shaded areas), suggesting that a substantial fraction of quasars tend to reside in more concentrated galaxies. Note that our classification of galaxy type is based on morphology, instead of star formation activity, as commonly practiced in the literature when studying the mass-size relation (e.g., van der Wel et al. 2014 used the UVJ diagram to distinguish early-type from late-type galaxies). As Section 5.1 will show, our quasars indeed have high SFRs and are predominately located on and above the galaxy star-forming MS. In this respect, we may regard our sample as comprising compact star-forming galaxies, similar to AGNs found at similar and higher redshifts (e.g., Barro et al. 2014; Kocevski et al. 2017; Silverman et al. 2019; Li et al. 2021a; Stacey et al. 2021).

We do not find a significant secondary dependence of the scatter of the $M_* - R_e$ relation with L_{bol} , M_{BH} , or λ_{E} . This suggests that quasars do not have a direct, instantaneous impact on host galaxy size, as might be expected for scenarios of AGN feedback that involve rapid and extensive gas expulsion (Fan et al. 2008, 2010). On the contrary, nearby quasars have an abundant cold gas reservoir (e.g., Husemann et al. 2017; Shangguan et al. 2018; Jarvis et al. 2020; Shangguan et al. 2020a; Koss et al. 2021), which is compact (Molina et al. 2021) and participates in vigorous (Xie et al. 2021), centrally concentrate star formation (Zhuang & Ho 2020).

5. IMPLICATIONS

5.1. Quasar Hosts and the Star-forming Main Sequence

The location of the host galaxies of quasars on the star-forming MS provides important clues regarding the possible connection between BH accretion and galaxy evolution. Existing studies, as discussed in Section 1, present a rather bewildering assortment of conflicting results. With the stellar masses in hand, the present sample, on account not only of its size but also the robust SFR measurements from Zhuang & Ho (2020), offers an opportunity to examine the nature of the star-forming MS for active galaxies (Figure 17). As a benchmark for comparison with the general galaxy population, we adopt the MS and its redshift evolution from Popesso et al. (2019a,b). Conservatively setting the scatter to ± 0.4 dex (width of 0.8 dex), the fraction of quasars that lie on or above the above is 43% (132/305) and 50% (151/305), respectively; and only 7% (22/305) sit below the MS. This

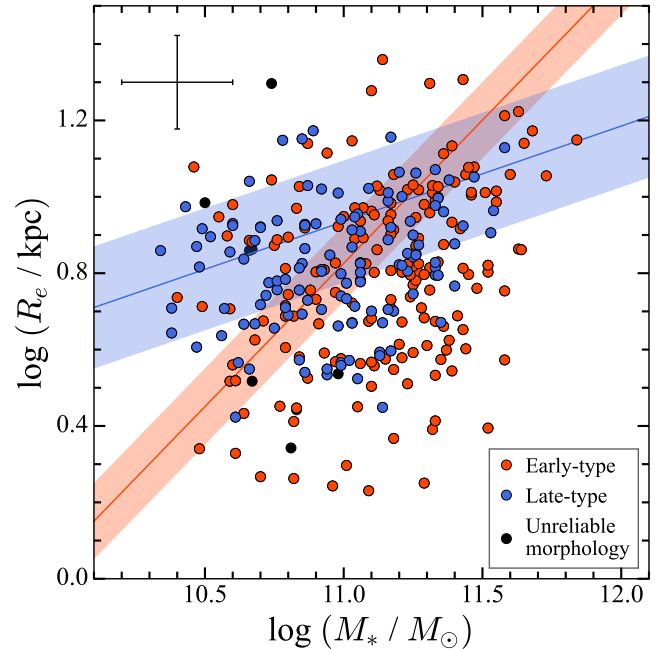


Figure 16. Relation between stellar mass (M_*) and effective radius (R_e) of AGN host galaxies of early-type (red), late-type (blue), and unreliable morphology (black). Blue and red lines represent the relations of early-type and late-type galaxies at redshift 0.25 from van der Wel et al. (2014), with shaded area indicating the intrinsic scatter of R_e from their fits. Typical uncertainties are shown in the upper-left corner.

result is robust against the choice of the MS used for comparison. For example, if we adopt the steeper MS relation of Speagle et al. (2014), which increases the SFR across the entire M_* range covered here, $\sim 85\%$ of the quasars are still located on or above the MS. Defining the distance to the galaxy star-forming MS as $\Delta\text{MS} \equiv \log \text{SFR} - \log \text{SFR}_{\text{MS}}$, ΔMS positively correlates with both M_{BH} and λ_{E} (Figure 18), indicating a close connection between BH accretion in the innermost regions of the galaxy and star formation activity on much larger scales.

There have been numerous attempts to quantify the connection between BH accretion and star formation activity. The situation is complex and depends strongly on sample selection (Section 1). Recent studies have emphasized the correlation between host galaxy SFR and the luminosity (or mass accretion rate) and Eddington ratio of the AGN, a trend reported in samples with diverse levels of AGN activity (e.g., Chen et al. 2013; Dai et al. 2018; Woo et al. 2020), including that from which the current study is drawn (Zhuang & Ho 2020). The results in Figure 17 bear a close resemblance to the situation for low-redshift ($\lesssim 0.5$) Palomar-Green quasars, many of which form stars prodigiously enough to qualify as starburst systems based on their star formation efficiencies (gas depletion timescales) and offset above the MS (Shang-

⁵ Because the i band corresponds to rest-frame $\sim 5700 \text{ \AA}$ at redshift 0.3, we do not apply any correction to the galaxy sizes given by van der Wel et al. (2014) which have already been converted to rest-frame 5000 \AA .

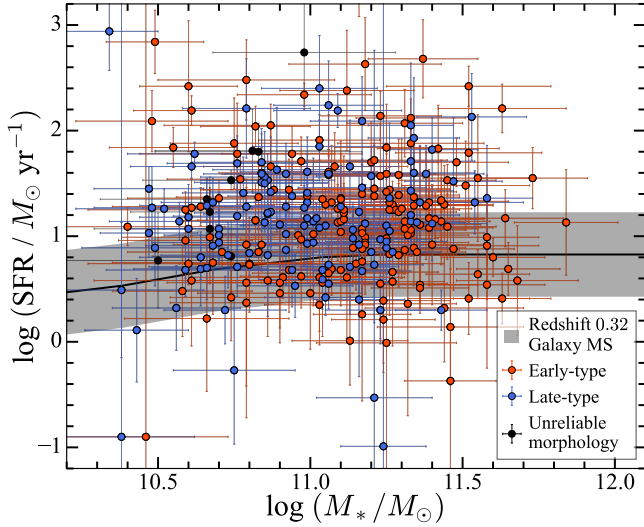


Figure 17. Comparison of star formation rate (SFR) versus stellar mass (M_*) of our redshift ~ 0.32 quasar sample with the galaxy MS at redshift 0.32 from Popesso et al. (2019a,b), shown as a black curve whose grey-shaded stripe (± 0.4 dex) indicates the width of the MS. AGN host galaxies are color-coded by their morphology: early-type (red), late-type (blue), and unreliable morphology (black).

guan et al. 2020a,b; Xie et al. 2021). Vigorous star formation goes hand-in-hand with BH accretion. But why? The connection may be largely indirect, a mere reflection of the fact that a common, contemporaneous gas supply is prerequisite to fuel both processes (e.g., Jarvis et al. 2020; Shangguan et al. 2020a; Yesuf & Ho 2020). In support of this interpretation, Zhuang et al. (2021) demonstrate that the strong correlation observed between \dot{M}_{BH} and SFR is driven mainly by the mutual dependence of these two parameters on molecular gas mass. Still, some investigators have argued that the two phenomena may be causally related. Star formation may be triggered directly by positive AGN feedback, as evidenced by the detection of in situ star formation in AGN-driven outflows and the tendency for the SFR in outflows to increase with higher mass outflow rate (e.g., Maiolino et al. 2017; Gallagher et al. 2019). More luminous AGNs exhibit more frequent and stronger outflows (e.g., Fiore et al. 2017; Rakshit & Woo 2018; Fluetsch et al. 2019; but see Shangguan et al. 2020b; Molina et al. 2022).

We remain agnostic on this unsettled debate. In our estimation, it is premature to judge which AGN property (\dot{M}_{BH} or λ_{E}), if any, is fundamentally correlated with enhanced star formation activity. As Zhuang & Ho (2020) show, current sample selection effects preclude us from obtaining truly independent estimates of \dot{M}_{BH} and λ_{E} : a relatively narrow range of M_{BH} can produce an artificial correlation between \dot{M}_{BH} and λ_{E} , and thus their correlation with ΔMS . AGN

samples with larger dynamical ranges in M_{BH} , \dot{M}_{BH} , and λ_{E} are required to fully investigate these issues.

5.2. Host Galaxy Morphology

Within our sample, the relative fraction of early-type and late-type hosts depends only on stellar mass, not on AGN properties such as L_{bol} and λ_{E} . While the two types of hosts differ significantly ($p \approx 10^{-4}$) according to the two-sample Kolmogorov-Smirnov test, they are very similar ($p > 0.2$) in terms of L_{bol} and λ_{E} (Figure 19). Dividing the sample according to the median stellar mass of $M_* = 10^{11} M_{\odot}$, we find that the fraction of quasars hosted in late-type galaxies drops from 50% in less massive systems to $\sim 30\%$ in the more massive bin. Approximately 70% of the AGNs live in early-type galaxies, qualitatively resembling the demographics of the host galaxies of less powerful AGNs (Ho et al. 1997; Kauffmann et al. 2003). The preference for quasars to reside in massive, bulge-dominated systems, of course, simply reflects the close link between BHs and galactic bulges.

However, disk-dominated hosts are still quite prevalent. They make up $\sim 40\%$ of the entire sample, and as much as $\sim 50\%$ of the objects with $M_* \lesssim 10^{11} M_{\odot}$. These results, together with the lack of correlation between galaxy morphology and the level of AGN activity, contributes to the long-standing debate on the triggering mechanism of AGNs. While gas-rich major mergers offer a natural framework to unify many aspects of AGNs and their host galaxies (e.g., Hopkins et al. 2008; Alexander & Hickox 2012), it has become increasingly recognized that more commonplace, less violent processes, such as minor mergers and stochastic gas accretion from bar and disk instability (Kormendy & Kennicutt 2004; Steinborn et al. 2018), suffice to fuel most of the gamut of AGN activity (e.g., Ho 2009; Cisternas et al. 2011; Villforth et al. 2017; Zhao et al. 2022). Indeed, a large fraction of nearby luminous AGNs are hosted in barred galaxies (e.g., Kim et al. 2017; Zhao et al. 2019, 2021). To the extent that major mergers destroy disks (Toomre & Toomre 1972; Barnes & Hernquist 1996), and even if under some circumstances disks can survive (Hopkins et al. 2009) or reform (Scannapieco et al. 2009), the sizable fraction of disk-dominated galaxies in our sample constitutes additional evidence of the secondary importance of major mergers in regulating AGN activity, even for the relatively high luminosities contained in our sample (median $L_{\text{bol}} = 10^{45.4} \text{ erg s}^{-1}$). Recent cosmological simulations find that the fraction of AGNs triggered by mergers is not enhanced in massive ($M_* > 10^{11} M_{\odot}$) galaxies, and that powerful AGNs are not more likely to be found in mergers compared to inactive galaxies (e.g., Steinborn et al. 2018; McAlpine et al. 2020; Sharma et al. 2022). Mergers contribute $\lesssim 40\%$ to the growth of both the central BH and the bulge in galaxies of $M_* \approx 10^{11} M_{\odot}$, highlighting the importance of gas fueling by secular pro-

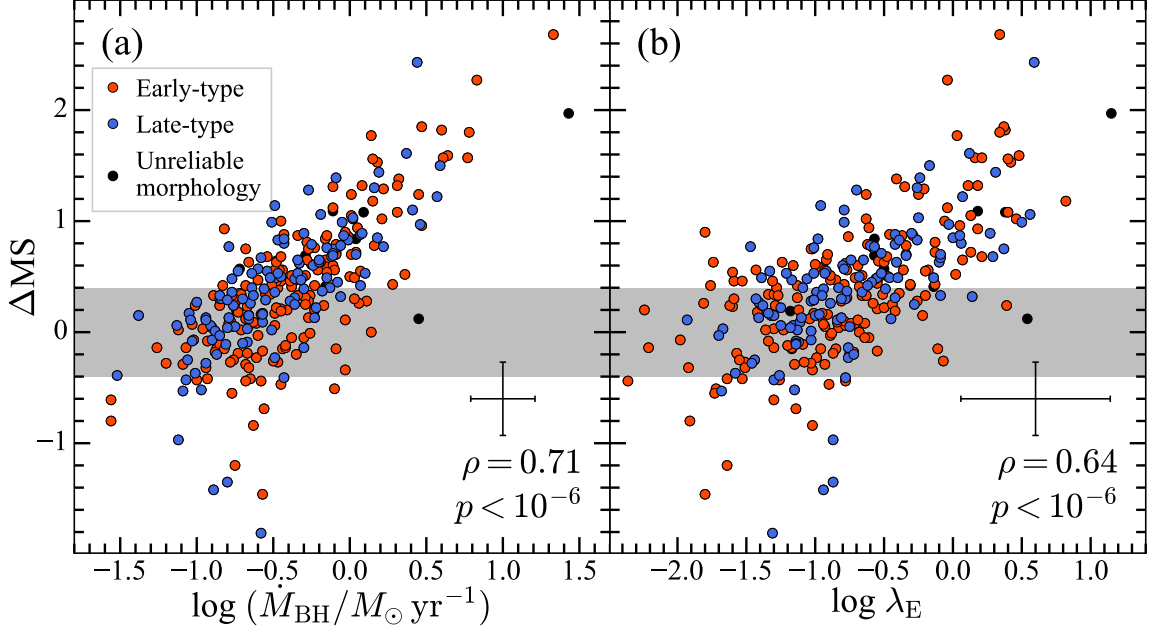


Figure 18. Distance to the galaxy star-forming main sequence ($\Delta_{\text{MS}} \equiv \log \text{SFR} - \log \text{SFR}_{\text{MS}}$) versus (a) BH accretion rate and (b) Eddington ratio with colors indicating their morphology: early-type (red), late-type (blue), and unreliable morphology (black). The lower-right corner of each panel shows the typical uncertainties and the Spearman correlation strength (ρ) and p -value for the whole sample. The grey-shaded stripe (± 0.4 dex) indicates the width of the MS at redshift 0.32 from [Popesso et al. \(2019a,b\)](#).

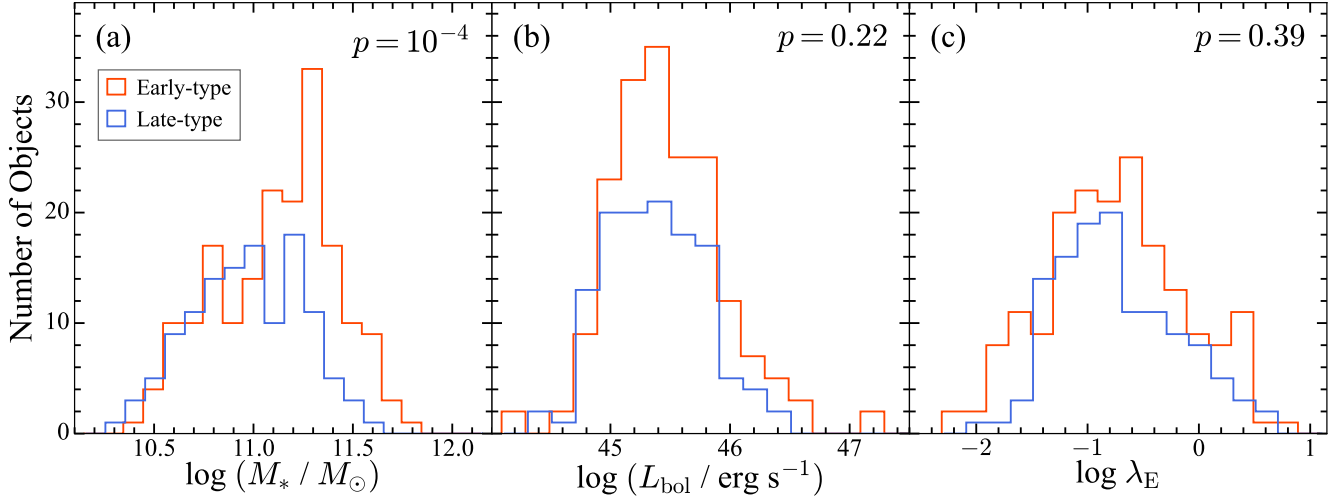


Figure 19. Distribution of (a) stellar mass, (b) AGN bolometric luminosity, and (c) Eddington ratio for early-type (red) and late-type (blue) galaxies. The p -value from the two-sample Kolmogorov-Smirnov test is shown in the upper-right corner of each panel.

cesses to the coevolution of supermassive BHs and their host galaxies (e.g., [Parry et al. 2009](#); [Martin et al. 2018](#); [McAlpine et al. 2020](#)).

The issue of the role of major mergers gains additional relevance owing to the large population of sources that lie significantly above the star-forming galaxy MS (Figure 17). Such clear-cut starburst systems, especially in view of the large masses involved ($M_* \approx 10^{11.0 \pm 0.5} M_\odot$), ordinarily would be associated with unambiguous, gas-rich major merg-

ers (e.g., [Petty et al. 2014](#); [Shangguan et al. 2019](#)). Our results do not conform to this expectation, judging by the broad representation of late-type galaxies among the population of Δ_{MS} sources.

6. SUMMARY

We perform two-dimensional, simultaneous, multiwavelength image decomposition of Pan-STARRS1 *grizy* images of 453 redshift ~ 0.3 quasars, the largest sample studied to

date, by explicitly considering the wavelength-dependence of galaxy structure. We obtain robust five-band photometry, structural parameters (half-light radii, Sérsic indices), and morphological classifications. Analysis of mock AGNs generated from both idealized and real galaxy images allows us to assess the uncertainties and systematic biases of the image decomposition. We combine SFRs from Zhuang & Ho (2020) with stellar masses derived from SED fitting of the multi-band photometry to investigate the star formation activity of quasar host galaxies in the context of the galaxy star-forming main sequence.

Our main results are as follows:

- The vast majority of the objects ($\sim 90\%$) are located on or above the galaxy star-forming main sequence. The distance to the main sequence positively correlates with BH accretion rate and Eddington ratio, with more rapidly accreting BHs exhibiting larger departures above the main sequence. This suggests a possible connection between BH accretion and star formation activity on galactic scales, but we caution against over-interpretation in view of their mutual dependence on gas supply.
- Using properly matched galaxies selected from the HST COSMOS field that have independently derived morphological types as a calibration sample, we classify our quasar hosts into late-type (39%) and early-type (58%) galaxies. The high fraction of late-type hosts, in conjunction with the lack of a clear dependence between host morphology and AGN properties, highlights the importance of internal secular processes in regulating AGN activity.
- While the majority of quasar host galaxies roughly follow the stellar mass-size relation of inactive galaxies,

both for late-type and early-type galaxies, $\sim 1/3$ of the quasar hosts fall below the $M_* - R_e$ relation. Together with the evidence for intense star formation, the host galaxies of nearby quasars structurally resemble compact star-forming galaxies at higher redshift.

This paper demonstrates the feasibility and tremendous potential of simultaneous multiwavelength image decomposition of nearby and even moderately distant galaxies, including those with strong nuclear activity. Apart from deep existing imaging surveys such as SDSS Stripe 82, Pan-STARRS1, and the Hyper Suprime-Cam Subaru Strategic Program, we can look forward to the upcoming Legacy Survey of Space and Time (LSST; Ivezić et al. 2019) of the Vera C. Rubin Observatory.

- 1 We thank the anonymous referee and Yingjie Peng for helpful
- 2 suggestions. This work was supported by the National Sci-
- 3 ence Foundation of China (11721303, 11991052, 12192220,
- 4 and 12192222) and the China Manned Space Project (CMS-
- 5 CSST-2021-A04 and CMS-CSST-2021-A06).

Software: Astropy (Astropy Collaboration et al. 2013, 2018), CIGALE (Boquien et al. 2019), GALFIT (Peng et al. 2002, 2010), GALFITM (Häußler et al. 2013; Vika et al. 2013), Matplotlib (Hunter 2007), Numpy (Harris et al. 2020), photutils (Bradley et al. 2020), PSFEX (Bertin 2011), reproject (<https://reproject.readthedocs.io/en/stable/index.html>), SExtractor (Bertin & Arnouts 1996), SWarp (Bertin et al. 2002)

APPENDIX

A. IMAGE DECOMPOSITION RESULTS

We show examples of decomposition results of two AGNs with the lowest (0.60) and highest (1.23) χ^2_ν in the final sample of 305 objects. Results for the entire sample can be found at <https://doi.org/10.12149/101130>.

B. TESTS FOR SEPARATE SINGLE-BAND DECOMPOSITION

AGN host galaxies images are usually analyzed one band at a time. When more than one band is being considered, it is common practice to fix certain parameters of the model based on the results obtained from another band (e.g., Zhao et al. 2021). In this Appendix, we compare the results of this

traditional approach with those of our new strategy of performing simultaneous, multiwavelength decomposition. As in Section 3.2.1, we perform mock tests using a set of galaxies selected from the COSMOS field. We first fit the i -band image independently with a nucleus plus Sérsic model. Then, fixing the best-fit position, structural (R_e , n), and geometric (position angle, axis ratio) parameters, we fit the same two-component model separately to the images of each of the other four ($grzy$) bands, allowing only the flux normalization to vary. The results for $m_{\text{Sérsic}}$ for the five bands are given

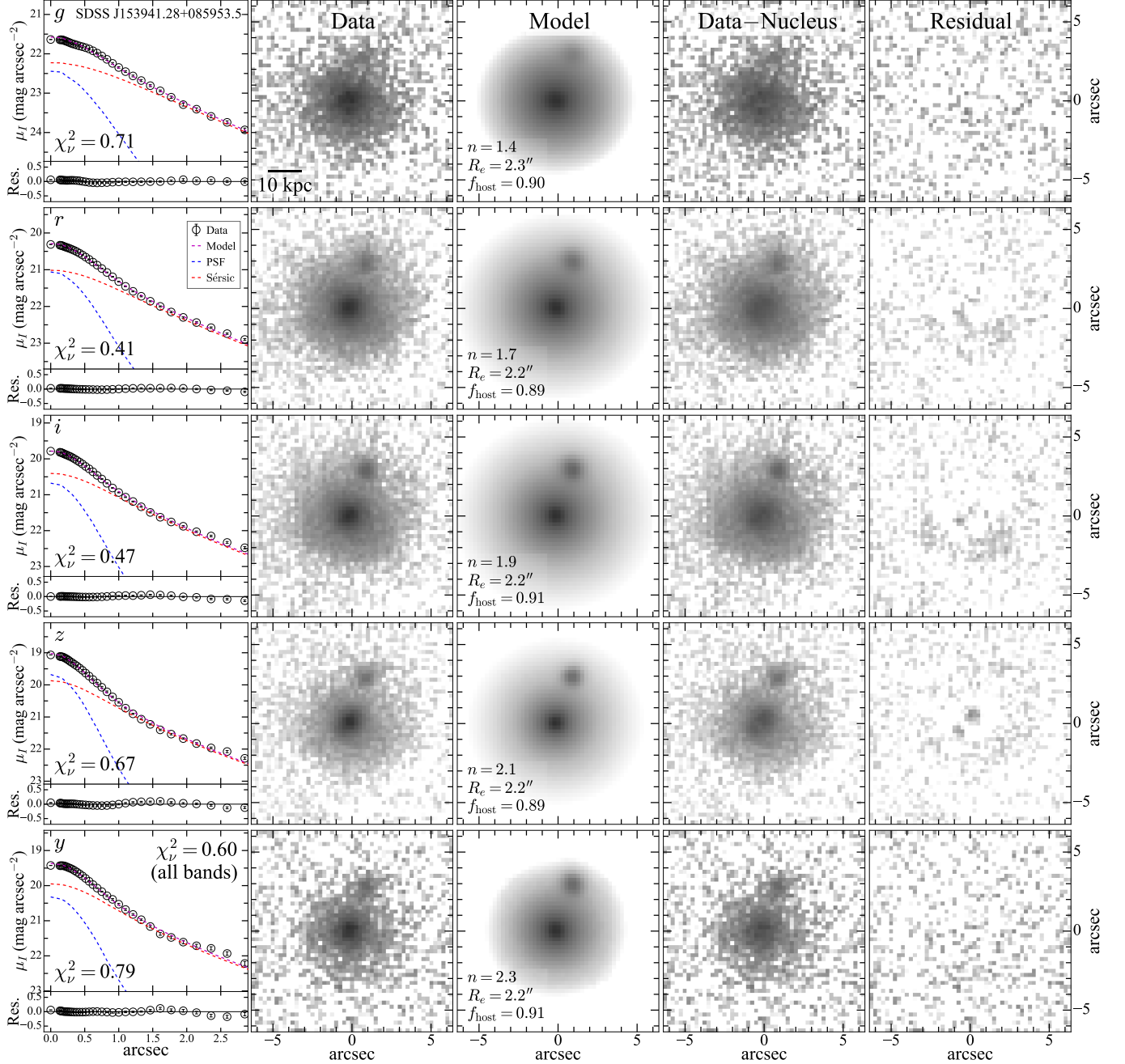


Figure A1. Same as in Figure 4, but for SDSS J153941.28+085953.5 (redshift 0.324), which has the lowest χ_ν^2 in the final sample.

in Figure A3, and Figure A4 assesses n and R_e , highlighting only the results for the i band.

The statistical results, averaged over the 16th, 50th, and 84th percentiles of AGN strength, are given Table A1, which summarizes the median difference, scatter, and detection fraction (fraction of objects with value at least 3 times its error) for both simultaneous multiwavelength decomposition (Section 3.2.1) and for separate single-band decomposition (this Appendix). While single-band decomposition still yields useful results, its overall performance, as judged by

either the absolute median difference or scatter, is worse than that of simultaneous multiwavelength decomposition. The most notable advantage of simultaneous multiwavelength decomposition lies in its significantly higher success rate of returning reliable detections.

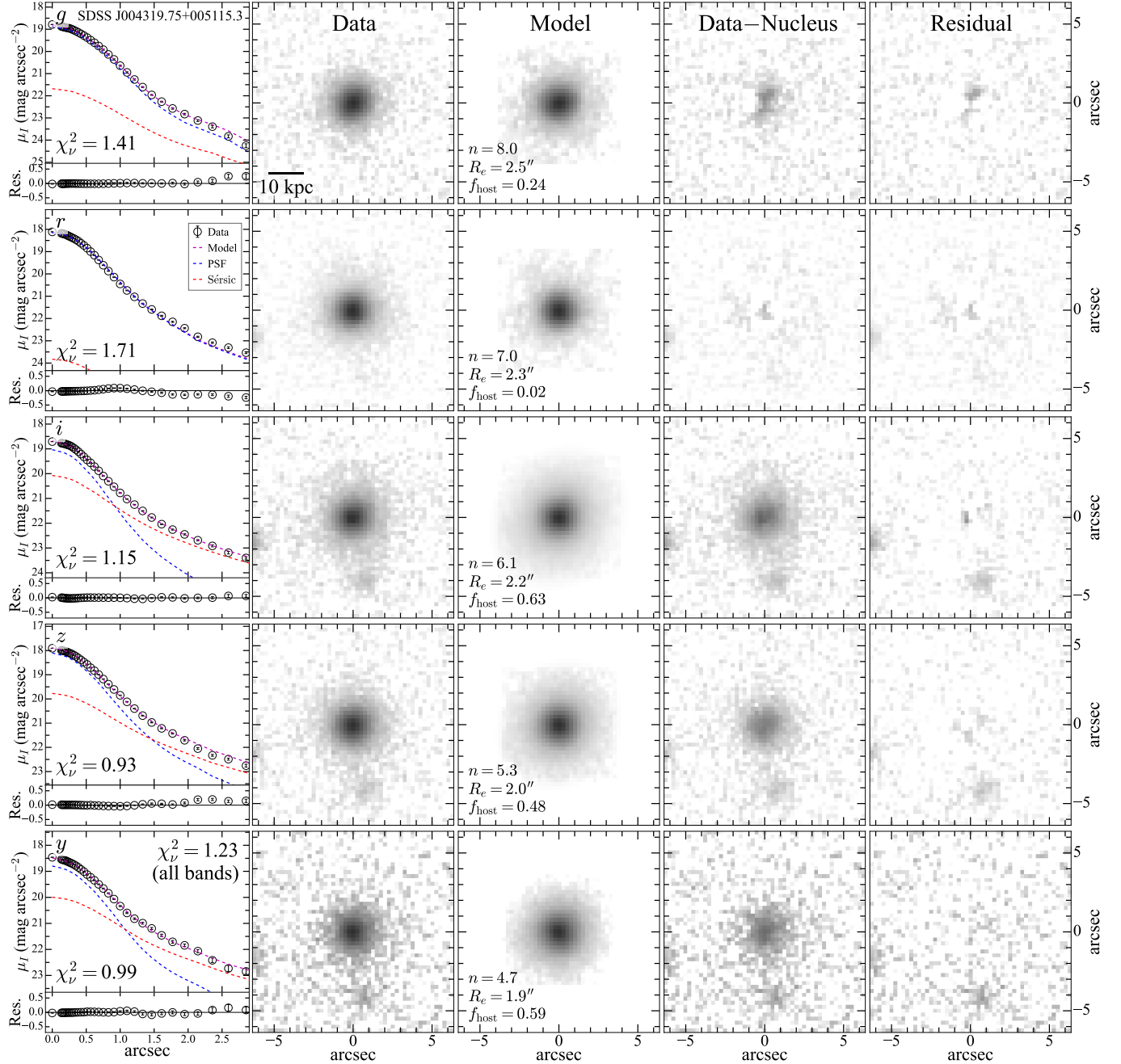


Figure A2. Same as in Figure 4, but for SDSS J004319.75+005115.3 (redshift 0.308), which has the highest χ^2_ν in the final sample.

REFERENCES

- Aihara, H., Arimoto, N., Armstrong, R., et al. 2018, PASJ, 70, S4
 Alexander, D. M., & Hickox, R. C. 2012, NewAR, 56, 93
 Anderson, J., & King, I. R. 2000, PASP, 112, 1360
 Annis, J., Soares-Santos, M., Strauss, M. A., et al. 2014, ApJ, 794, 120
 Astropy Collaboration, Price-Whelan, A. M., Sipőcz, B. M., et al. 2018, AJ, 156, 123
 Astropy Collaboration, Robitaille, T. P., Tollerud, E. J., et al. 2013, A&A, 558, A33
 Barnes, J. E., & Hernquist, L. E. 1996, ApJ, 471, 115
 Barro, G., Faber, S. M., Pérez-González, P. G., et al. 2014, ApJ, 791, 52
 Bell, E. F., McIntosh, D. H., Katz, N., & Weinberg, M. D. 2003, ApJS, 149, 289
 Bennert, V. N., Treu, T., Ding, X., et al. 2021, ApJ, 921, 36
 Bentz, M. C., & Manne-Nicholas, E. 2018, ApJ, 864, 146

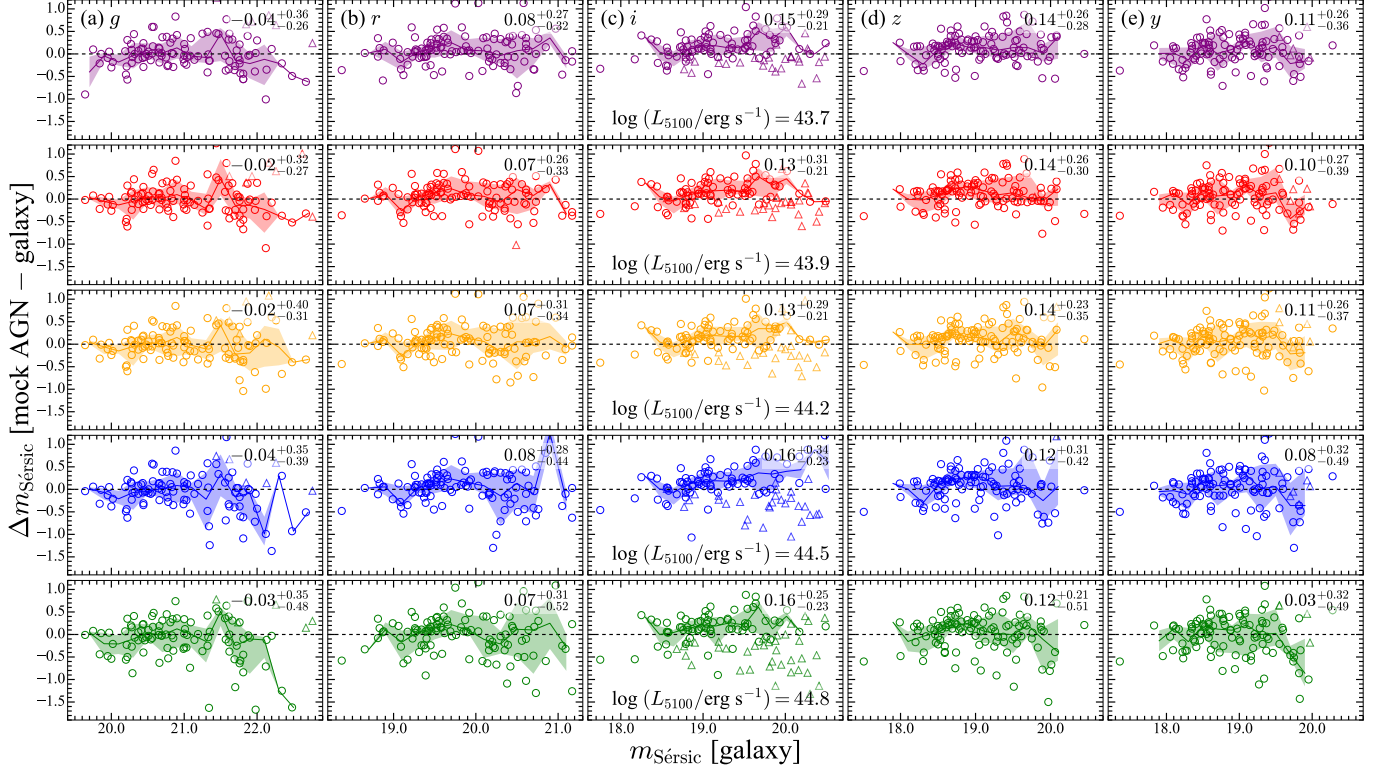


Figure A3. Same as in Figure 8, but for $m_{\text{Sérsic}}$ obtained using separate, GALFIT single-band fits, fixing the structure of the galaxy to that derived in the i band.

Table A1. Statistical Comparison of Two Methods of Decomposition

Statistics	$m_{\text{Sérsic}} [g]$	$m_{\text{Sérsic}} [r]$	$m_{\text{Sérsic}} [i]$	$m_{\text{Sérsic}} [z]$	$m_{\text{Sérsic}} [y]$	$\log n$	$\log R_e$
	(mag)	(mag)	(mag)	(mag)	(mag)		(pixel)
<i>Simultaneous Multiwavelength Decomposition</i>							
Median	0.09	-0.02	0.03	0.04	0.08	-0.08	0.00
Scatter	0.30	0.25	0.19	0.19	0.19	0.21	0.12
Detection fraction	61%	78%	86%	82%	70%	65%	77%
<i>Separate Single-band Decomposition</i>							
Median	-0.03	0.07	0.14	0.13	0.10	-0.22	0.04
Scatter	0.34	0.33	0.27	0.31	0.35	0.20	0.11
Detection fraction	72%	43%	67%

NOTE—Statistics are averaged over the 16th, 50th, and 84th percentiles of AGN strength.

Berriman, G. B., Good, J. C., Laity, A. C., & Kong, M. 2008, in ASP Conf. Ser. 394, *Astronomical Data Analysis Software and Systems XVII*, ed. R. W. Argyle, P. S. Bunclark, & J. R. Lewis (San Francisco: ASP), 83

Bertin, E. 2011, in ASP Conf. Ser. 442, *Astronomical Data Analysis Software and Systems XX*, ed. I. N. Evans, A. Accomazzi, D. J. Mink, & A. H. Rots (San Francisco: ASP), 435

Bertin, E., & Arnouts, S. 1996, *A&AS*, 117, 393

Bertin, E., Mellier, Y., Radovich, M., et al. 2002, in ASP Conf. Ser. 281, *Astronomical Data Analysis Software and Systems XI*, ed. D. A. Bohlender, D. Durand, & T. H. Handley (San Francisco: ASP), 228

Birrer, S., & Amara, A. 2018, *Physics of the Dark Universe*, 22, 189

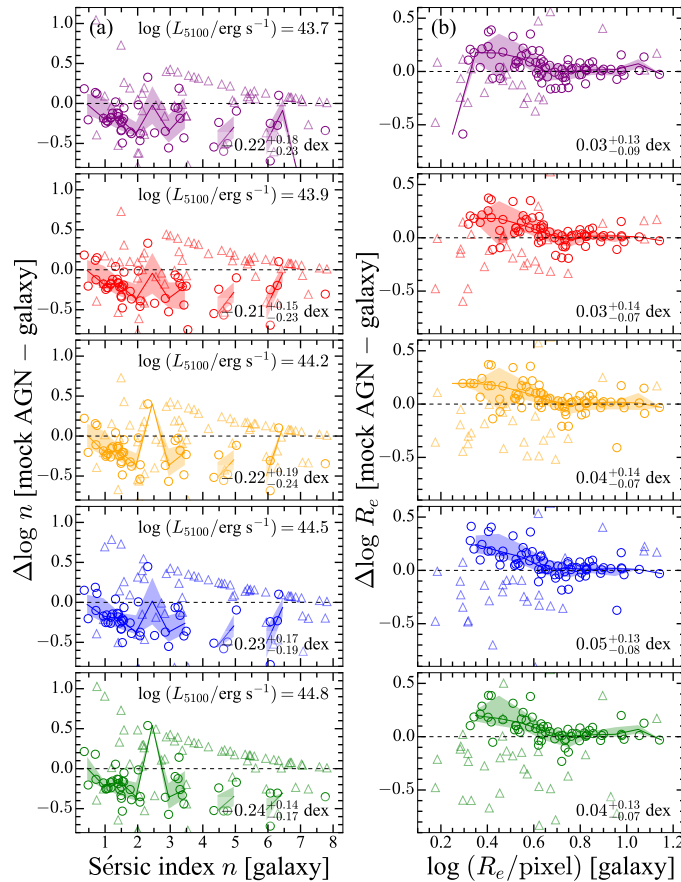


Figure A4. Same as in Figure 9, but for the Sérsic index n and half-light radius (R_e) obtained from GALFIT decomposition of the i -band image of the mock AGNs.

Boquien, M., Burgarella, D., Roehly, Y., et al. 2019, *A&A*, 622, A103
Bradley, L., Sipőcz, B., Robitaille, T., et al. 2020, *astropy/photutils*: 1.0.1, 1.0.1, Zenodo
Brinchmann, J., Charlot, S., White, S. D. M., et al. 2004, *MNRAS*, 351, 1151
Brüggen, M., & Kaiser, C. R. 2002, *Nature*, 418, 301
Bruzual, G., & Charlot, S. 2003, *MNRAS*, 344, 1000
Calistro Rivera, G., Lusso, E., Hennawi, J. F., et al. 2016, *ApJ*, 833, 98
Calzetti, D., Armus, L., Bohlin, R. C., et al. 2000, *ApJ*, 533, 682
Chabrier, G. 2003, *PASP*, 115, 763
Chambers, K. C., Magnier, E. A., Metcalfe, N., et al. 2016, arXiv:1612.05560
Chen, C.-T. J., Hickox, R. C., Alberts, S., et al. 2013, *ApJ*, 773, 3
Ciesla, L., Charmandaris, V., Georgakakis, A., et al. 2015, *A&A*, 576, A10
Cisternas, M., Jahnke, K., Inskip, K. J., et al. 2011, *ApJ*, 726, 57
Conroy, C. 2013, *ARA&A*, 51, 393
Cresci, G., Mainieri, V., Brusa, M., et al. 2015, *ApJ*, 799, 82
Dai, Y. S., Wilkes, B. J., Bergeron, J., et al. 2018, *MNRAS*, 478, 4238

Davari, R., Ho, L. C., Mobasher, B., & Canalizo, G. 2017, *ApJ*, 836, 75
Di Matteo, T., Springel, V., & Hernquist, L. 2005, *Nature*, 433, 604
Ding, X., Silverman, J., Treu, T., et al. 2020, *ApJ*, 888, 37
Dunlop, J. S., McLure, R. J., Kukula, M. J., et al. 2003, *MNRAS*, 340, 1095
Elbaz, D., Dickinson, M., Hwang, H. S., et al. 2011, *A&A*, 533, A119
Ellison, S. L., Teimoorinia, H., Rosario, D. J., & Mendel, J. T. 2016, *MNRAS*, 458, L34
Erwin, P. 2015, *ApJ*, 799, 226
Falomo, R., Bettoni, D., Karhunen, K., Kotilainen, J. K., & Uslenghi, M. 2014, *MNRAS*, 440, 476
Fan, L., Lapi, A., Bressan, A., et al. 2010, *ApJ*, 718, 1460
Fan, L., Lapi, A., De Zotti, G., & Danese, L. 2008, *ApJL*, 689, L101
Farrow, D. J., Cole, S., Metcalfe, N., et al. 2014, *MNRAS*, 437, 748
Ferrarese, L., & Merritt, D. 2000, *ApJ*, 539, L9
Feruglio, C., Maiolino, R., Piconcelli, E., et al. 2010, *A&A*, 518, L155
Fiore, F., Feruglio, C., Shankar, F., et al. 2017, *A&A*, 601, A143

- Flewelling, H. A., Magnier, E. A., Chambers, K. C., et al. 2020, *ApJS*, 251, 7
- Fluetsch, A., Maiolino, R., Carniani, S., et al. 2019, *MNRAS*, 483, 4586
- Gabor, J. M., Impey, C. D., Jahnke, K., et al. 2009, *ApJ*, 691, 705
- Gallagher, R., Maiolino, R., Belfiore, F., et al. 2019, *MNRAS*, 485, 3409
- Gao, H., & Ho, L. C. 2017, *ApJ*, 845, 114
- Gao, H., Ho, L. C., Barth, A. J., & Li, Z.-Y. 2019, *ApJS*, 244, 34
- Gebhardt, K., Bender, R., Bower, G., et al. 2000, *ApJ*, 539, L13
- Green, G. M. 2018, *The Journal of Open Source Software*, 3, 695
- Greene, J. E., Ho, L. C., & Barth, A. J. 2008, *ApJ*, 688, 159
- Harris, C. R., Millman, K. J., van der Walt, S. J., et al. 2020, *Nature*, 585, 357
- Häußler, B., Bamford, S. P., Vika, M., et al. 2013, *MNRAS*, 430, 330
- Häußler, B., McIntosh, D. H., Barden, M., et al. 2007, *ApJS*, 172, 615
- Heckman, T. M., & Best, P. N. 2014, *ARA&A*, 52, 589
- Ho, L. C. 2004, ed., *Carnegie Observatories Astrophysics Series*, Vol. 1: Coevolution of Black Holes and Galaxies (Cambridge: Cambridge Univ. Press)
- Ho, L. C. 2005, *ApJ*, 629, 680
- Ho, L. C. 2008, *ARA&A*, 46, 475
- Ho, L. C. 2009, *ApJ*, 699, 626
- Ho, L. C., Filippenko, A. V., & Sargent, W. L. W. 1997, *ApJ*, 487, 568
- Ho, L. C., Filippenko, A. V., & Sargent, W. L. W. 2003, *ApJ*, 583, 159
- Hönig, S. F. & Kishimoto, M. 2017, *ApJL*, 838, L20
- Hopkins, P. F., Cox, T. J., Younger, J. D., & Hernquist, L. 2009, *ApJ*, 691, 1168
- Hopkins, P. F., Hernquist, L., Cox, T. J., & Kereš, D. 2008, *ApJS*, 175, 356
- Hunter, J. D. 2007, *Computing in Science & Engineering*, 9, 90
- Husemann, B., Davis, T. A., Jahnke, K., et al. 2017, *MNRAS*, 470, 1570
- Husemann, B., Jahnke, K., Sánchez, S. F., et al. 2014, *MNRAS*, 443, 755
- Ishino, T., Matsuoka, Y., Koyama, S., et al. 2020, *PASJ*, 72, 83
- Ivezić, Ž., Kahn, S. M., Tyson, J. A., et al. 2019, *ApJ*, 873, 111
- Jarvis, M. E., Harrison, C. M., Mainieri, V., et al. 2020, *MNRAS*, 498, 1560
- Jiang, Y.-F., Greene, J. E., Ho, L. C., Xiao, T., & Barth, A. J. 2011, *ApJ*, 742, 68
- Kauffmann, G., Heckman, T. M., Tremonti, C., et al. 2003, *MNRAS*, 346, 1055
- Kelvin, L. S., Driver, S. P., Robotham, A. S. G., et al. 2012, *MNRAS*, 421, 1007
- Kim, M., Barth, A. J., Ho, L. C., & Son, S. 2021, *ApJS*, 256, 40
- Kim, M., & Ho, L. C. 2019, *ApJ*, 876, 35
- Kim, M., Ho, L. C., & Im, M. 2006, *ApJ*, 642, 702
- Kim, M., Ho, L. C., Peng, C. Y., Barth, A. J., & Im, M. 2008, *ApJS*, 179, 283
- Kim, M., Ho, L. C., Peng, C. Y., Barth, A. J., & Im, M. 2017, *ApJS*, 232, 21
- Kocevski, D. D., Barro, G., Faber, S. M., et al. 2017, *ApJ*, 846, 112
- Koekemoer, A. M., Aussel, H., Calzetti, D., et al. 2007, *ApJS*, 172, 196
- Kormendy, J., & Ho, L. C. 2013, *ARA&A*, 51, 511
- Kormendy, J., & Kennicutt Jr., R. C., 2004, *ARA&A*, 42, 603
- Koss, M. J., Strittmatter, B., Lamperti, I., et al. 2021, *ApJS*, 252, 29
- Koutoulidis, L., Mountrichas, G., Georgantopoulos, I., et al. 2022, *A&A*, 658, A35
- Kron, R. G. 1980, *ApJS*, 43, 305
- Kroupa, P. 2001, *MNRAS*, 322, 231
- Laigle, C., McCracken, H. J., Ilbert, O., et al. 2016, *ApJS*, 224, 24
- Leslie, S. K., Kewley, L. J., Sanders, D. B., & Lee, N. 2016, *MNRAS*, 455, L82
- Li, J., Silverman, J. D., Ding, X., et al. 2021a, *ApJ*, 918, 22
- Li, J. I.-H., Shen, Y., Ho, L. C., et al. 2021b, *ApJ*, 906, 103
- Lilly, S. J., Le Brun, V., Maier, C., et al. 2009, *ApJS*, 184, 218
- Liu, H.-Y., Liu, W.-J., Dong, X.-B., et al. 2019, *ApJS*, 243, 21
- Madau, P., & Dickinson, M. 2014, *ARA&A*, 52, 415
- Magorrian, J., Tremaine, S., Richstone, D., et al. 1998, *AJ*, 115, 2285
- Maiolino, R., Russell, H. R., Fabian, A. C., et al. 2017, *Nature*, 544, 202
- Mandal, A., Mukherjee, D., Federrath, C., et al. 2021, *MNRAS*, 508, 4738
- Martin, G., Kaviraj, S., Volonteri, M., et al. 2018, *MNRAS*, 476, 2801
- Matsuoka, Y., Strauss, M. A., Price, Ted N., I., & DiDonato, M. S. 2014, *ApJ*, 780, 162
- Matsuoka, Y., Strauss, M. A., Shen, Y., et al. 2015, *ApJ*, 811, 91
- McAlpine, S., Harrison, C. M., Rosario, D. J., et al. 2020, *MNRAS*, 494, 5713
- McLure, R. J., Dunlop, J. S., Kukula, M. J., et al. 1999, *MNRAS*, 308, 377
- McNamara, B. R. & Nulsen, P. E. J. 2007, *ARA&A*, 45, 117
- Merloni, A., Bongiorno, A., Bolzonella, M., et al. 2010, *ApJ*, 708, 137
- Molina, J., Ho, L. C., Wang, R., et al. 2022, *ApJ*, submitted
- Molina, J., Wang, R., Shangguan, J., et al. 2021, *ApJ*, 908, 231
- Parry, O. H., Eke, V. R., & Frenk, C. S. 2009, *MNRAS*, 396, 1972
- Peng, C. Y., Ho, L. C., Impey, C. D., & Rix, H.-W. 2002, *AJ*, 124, 266
- Peng, C. Y., Ho, L. C., Impey, C. D., & Rix, H.-W. 2010, *AJ*, 139, 2097

- Peng, C. Y., Impey, C. D., Ho, L. C., Barton, E. J., & Rix, H.-W. 2006, *ApJ*, 640, 114
- Petty, S. M., Armus, L., Charmandaris, V., et al. 2014, *AJ*, 148, 111
- Popesso, P., Concas, A., Morselli, L., et al. 2019a, *MNRAS*, 483, 3213
- Popesso, P., Morselli, L., Concas, A., et al. 2019b, *MNRAS*, 490, 5285
- Qiu, Y., Bogdanović, T., Li, Y., et al. 2020, *Nature Astronomy*, 4, 900
- Rakshit, S., & Woo, J.-H. 2018, *ApJ*, 865, 5
- Renzini, A., & Peng, Y.-j. 2015, *ApJL*, 801, L29
- Richards, G. T., Lacy, M., Storrie-Lombardi, L. J., et al. 2006, *ApJS*, 166, 470
- Richstone, D., Ajhar, E. A., Bender, R., et al. 1998, *Nature*, 395, A14
- Robotham, A. S. G., Taranu, D. S., Tobar, R., Moffett, A., & Driver, S. P. 2017, *MNRAS*, 466, 1513
- Salim, S., Rich, R. M., Charlot, S., et al. 2007, *ApJS*, 173, 267
- Scannapieco, C., White, S. D. M., Springel, V., & Tissera, P. B. 2009, *MNRAS*, 396, 696
- Scarlata, C., Carollo, C. M., Lilly, S., et al. 2007, *ApJS*, 172, 406
- Schlafly, E. F., & Finkbeiner, D. P. 2011, *ApJ*, 737, 103
- Schlegel, D. J., Finkbeiner, D. P., & Davis, M. 1998, *ApJ*, 500, 525
- Schmidt, M., & Green, R. F. 1983, *ApJ*, 269, 352
- Scoville, N., Aussel, H., Brusa, M., et al. 2007, *ApJS*, 172, 1
- Sérsic, J. L. 1968, *Atlas de Galaxias Australes* (Córdoba: Obs. Astron., Univ. Nac. Córdoba)
- Shangguan, J., Ho, L. C., Bauer, F. E., Wang, R., & Treister, E. 2020a, *ApJS*, 247, 15
- Shangguan, J., Ho, L. C., Bauer, F. E., Wang, R., & Treister, E. 2020b, *ApJ*, 899, 112
- Shangguan, J., Ho, L. C., Li, R., et al. 2019, *ApJ*, 870, 104
- Shangguan, J., Ho, L. C., & Xie, Y. 2018, *ApJ*, 854, 15
- Sharma, R. S., Choi, E., Somerville, R. S., et al. 2022, *ApJ*, submitted (arXiv:2101.01729)
- Shimizu, T. T., Mushotzky, R. F., Meléndez, M., Koss, M., & Rosario, D. J. 2015, *MNRAS*, 452, 1841
- Shin, J., Woo, J.-H., Chung, A., et al. 2019, *ApJ*, 881, 147
- Silverman, J. D., Treu, T., Ding, X., et al. 2019, *ApJL*, 887, L5
- Smirnova-Pinchukova, I., Husemann, B., Davis, T. A., et al. 2022, *A&A*, submitted (arXiv:2111.10419)
- Somerville, R. S., & Davé, R. 2015, *ARA&A*, 53, 51
- Speagle, J. S., Steinhardt, C. L., Capak, P. L., & Silverman, J. D. 2014, *ApJS*, 214, 15
- Stacey, H. R., McKean, J. P., Powell, D. M., et al. 2021, *MNRAS*, 500, 3667
- Stalevski, M., Tristram, K. R. W., & Asmus, D. 2019, *MNRAS*, 484, 3334
- Steinborn, L. K., Hirschmann, M., Dolag, K., et al. 2018, *MNRAS*, 481, 341
- Stemo, A., Comerford, J. M., Barrows, R. S., et al. 2020, *ApJ*, 888, 78
- Suh, H., Civano, F., Hasinger, G., et al. 2019, *ApJ*, 872, 168
- Thomas, A. D., Dopita, M. A., Kewley, L. J., et al. 2018, *ApJ*, 856, 89
- Toomre, A., & Toomre, J. 1972, *ApJ*, 178, 623
- Torbaniuk, O., Paolillo, M., Carrera, F., et al. 2021, *MNRAS*, 506, 2619
- Vanden Berk, D. E., Shen, J., Yip, C.-W., et al. 2006, *AJ*, 131, 84
- van der Wel, A., Bell, E. F., Häussler, B., et al. 2012, *ApJS*, 203, 24
- van der Wel, A., Franx, M., van Dokkum, P. G., et al. 2014, *ApJ*, 788, 28
- Vika, M., Bamford, S. P., Häußler, B., et al. 2013, *MNRAS*, 435, 623
- Villforth, C., Hamilton, T., Pawlik, M. M., et al. 2017, *MNRAS*, 466, 812
- Waters, C. Z., Magnier, E. A., Price, P. A., et al. 2020, *ApJS*, 251, 4
- Wild, V., Kauffmann, G., Heckman, T., et al. 2007, *MNRAS*, 381, 543
- Woo, J.-H., Son, D., & Bae, H.-J. 2017, *ApJ*, 839, 120
- Woo, J.-H., Son, D., & Rakshit, S. 2020, *ApJ*, 901, 66
- Xie, Y., Ho, L. C., Zhuang, M.-Y., & Shangguan, J. 2021, *ApJ*, 910, 124
- Yang, G., Boquien, M., Buat, V., et al. 2020, *MNRAS*, 491, 740
- Yesuf, H. M., & Ho, L. C. 2019, *ApJ*, 884, 177
- Yesuf, H. M., & Ho, L. C. 2020, *ApJ*, 901, 42
- York, D. G., Adelman, J., Anderson, Jr., J. E., et al. 2000, *AJ*, 120, 1579
- Yue, M., Jiang, L., Shen, Y., et al. 2018, *ApJ*, 863, 21
- Zhao, D., Ho, L. C., Zhao, Y., Shangguan, J., & Kim, M. 2019, *ApJ*, 877, 52
- Zhao, Y., Ho, L. C., Shangguan, J., et al. 2021, *ApJ*, 911, 94
- Zhao, Y., Li, Y. A., Shangguan, J., Zhuang, M.-Y., & Ho, L. C. 2022, *ApJ*, 925, 70
- Zhuang, M.-Y., & Ho, L. C. 2019, *ApJ*, 882, 89
- Zhuang, M.-Y., & Ho, L. C. 2020, *ApJ*, 896, 108
- Zhuang, M.-Y., Ho, L. C., & Shangguan, J. 2018, *ApJ*, 862, 118
- Zhuang, M.-Y., Ho, L. C., & Shangguan, J. 2019, *ApJ*, 873, 103
- Zhuang, M.-Y., Ho, L. C., & Shangguan, J. 2021, *ApJ*, 906, 38
- Zubovas, K., Nayakshin, S., King, A., et al. 2013, *MNRAS*, 433, 3079